

The complete far-infrared and submillimeter spectrum of the Class 0 protostar Serpens SMM1 obtained with *Herschel**[†]

Characterizing UV-irradiated shocks heating and chemistry

Javier R. Goicoechea¹, J. Cernicharo¹, A. Karska^{2,3}, G.J. Herczeg⁴, E. T. Polehampton^{5,6},
S. F. Wampfler⁷, L. E. Kristensen³, E.F. van Dishoeck^{2,3}, M. Etxaluze¹, O. Berne^{8,9}, R. Visser¹⁰

(Affiliations can be found after the references)

Submitted 28 June 2012; accepted 17 September 2012

ABSTRACT

We present the first complete $\sim 55\text{--}671\mu\text{m}$ spectral scan of a low-mass Class 0 protostar (Serpens SMM1) taken with the PACS and SPIRE spectrometers on board *Herschel*. More than 145 lines have been detected, most of them rotationally excited lines of ^{12}CO (full ladder from $J_u=4\text{--}3$ to $42\text{--}41$ and $E_u/k=4971\text{ K}$), H_2O (up to $8_{18}\text{--}7_{07}$ and $E_u/k=1036\text{ K}$), OH (up to $^2\Pi_{1/2}, J=7/2\text{--}5/2$ and $E_u/k=618\text{ K}$), ^{13}CO (up to $J_u=16\text{--}15$), HCN and HCO^+ (up to $J_u=12\text{--}11$). Bright [O I]63, 145 μm and weaker [C II]158 and [C I]370, 609 μm lines are also detected, but excited lines from chemically related species (NH_3 , CH^+ , CO^+ , OH^+ or H_2O^+) are not. Mid-IR spectra retrieved from the *Spitzer* archive are also first discussed here. The $\sim 10\text{--}37\mu\text{m}$ spectrum has many fewer lines, but shows clear detections of [Ne II], [Fe II], [Si II] and [S I] fine structure lines, as well as weaker $\text{H}_2\text{ S(1)}$ and S(2) pure rotational lines. The observed line luminosity is dominated by CO ($\sim 54\%$), H_2O ($\sim 22\%$), [O I] ($\sim 12\%$) and OH ($\sim 9\%$) emission. A multi-component radiative transfer model allowed us to approximately quantify the contribution of the three different temperature components suggested by the ^{12}CO rotational ladder ($T_k^{\text{hot}} \approx 800\text{ K}$, $T_k^{\text{warm}} \approx 375\text{ K}$ and $T_k^{\text{cool}} \approx 150\text{ K}$). Gas densities $n(\text{H}_2) \gtrsim 5 \times 10^6\text{ cm}^{-3}$ are needed to reproduce the observed far-IR lines arising from shocks in the inner protostellar envelope (*warm* and *hot* components) for which we derive upper limit abundances of $x(\text{CO}) \lesssim 10^{-4}$, $x(\text{H}_2\text{O}) \lesssim 0.2 \times 10^{-5}$ and $x(\text{OH}) \lesssim 10^{-6}$ with respect to H_2 . The lower energy submm ^{12}CO and H_2O lines show more extended emission that we associate with the *cool* entrained outflow gas. Fast dissociative J -shocks ($v_s > 60\text{ km s}^{-1}$) within an embedded atomic jet, as well as lower velocity small-scale non-dissociative shocks ($v_s \lesssim 20\text{ km s}^{-1}$) are needed to explain both the atomic fine structure lines and the *hot* CO and H_2O lines respectively. Observations also show the signature of UV radiation (weak [C II] and [C I] lines and high HCO^+/HCN abundance ratios) and thus, most observed species likely arise in UV-irradiated shocks. Dissociative J -shocks produced by a jet impacting the ambient material are the most probable origin of [O I] and OH emission and of a significant fraction of the *warm* CO emission. In addition, H_2O photodissociation in UV-irradiated non-dissociative shocks along the outflow cavity walls can also contribute to the [O I] and OH emission.

Key words. Stars: protostars; — infrared: ISM — ISM: jets and outflows — molecular processes — shock waves

1. Introduction

In the earliest stages of evolution, low-mass protostars are deeply embedded in dense envelopes of molecular gas and dust. During collapse, conservation of angular momentum combined with infall along the magnetic field lines leads to the formation of a dense rotating protoplanetary disk that drives the accretion process. At the same time, both mass and angular momentum are removed from the system by the onset of jets, collimated flows, and the magnetic braking action (e.g., Bontemps et al. 1996; Bachiller & Tafalla 1999). The resulting outflow produces a cavity in the natal envelope with walls subjected to energetic shocks and strong radiation fields from the protostar. These processes heat the circumstellar gas and leave their signature in the prevailing chemistry (e.g., enhanced abundances of water vapour).

Both the line and continuum emission from Young Stellar Objects (YSOs) peak in the far-infrared (far-IR) and thus they are robust diagnostics of the energetic processes associated with the first stages of star formation (e.g., Giannini et al. 2001). The improved sensitivity and angular/spectral resolution of *Herschel* spectrometers compared to previous far-IR observatories allows

us to detect a larger number of far-IR lines and to better constrain their spatial origin. This is especially true for the detection of high excitation, optically thin lines that can help us to identify high temperature components as well as to disentangle and quantify the dominant heating mechanisms (mechanical vs. radiative). Early *Herschel* observations of a few low-mass protostars for which partial or complete PACS spectra are available show that the molecular emission of relatively excited ^{12}CO ($J < 30$), H_2O and OH lines is a common feature (van Kempen et al. 2010 for HH46 and Benedettini et al. 2012 for L1157-B1). This *warm* CO and H_2O emission was suggested to arise from the walls of an outflow-carved cavity in the envelope, which are heated by UV photons and by non-dissociative *C*-type shocks (van Kempen et al. 2010; Visser et al. 2012). The [O I] and OH emission observed in these sources, however, was proposed to arise from dissociative J -shocks. Herczeg et al. (2012) detected higher- J ^{12}CO lines (up to $J=49\text{--}48$) and highly excited H_2O lines in the NGC 1333 IRAS 4B outflow indicating the presence of even hotter gas. The very weak [O I]63 μm line emission in IRAS 4B outflow (the [O I]145 μm line is not even detected) led these authors to conclude that the hot gas where H_2O dominates the gas cooling is heated by non-dissociative *C*-shocks shielded from UV radiation. Passive heating by the protostellar luminosity is also thought to contribute to the mid- J ^{12}CO and ^{13}CO

* *Herschel* is an ESA space observatory with science instruments provided by European-led Principal Investigator consortia and with important participation from NASA.

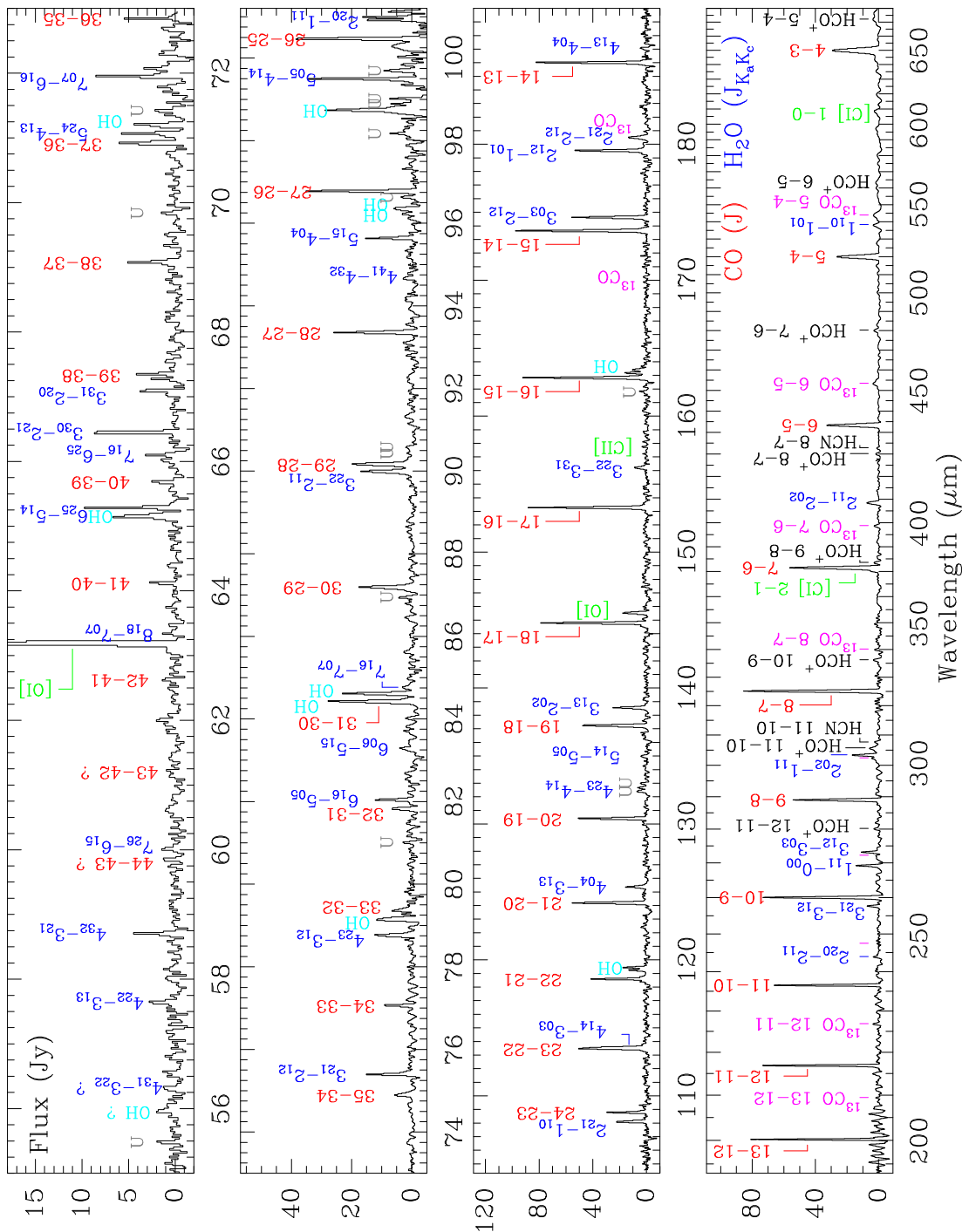


Fig. 1. PACS and SPIRE (lower panel) continuum-subtracted spectra of Serpens SMM1 (central spaxel) with H₂O (blue), CO (red), OH (cyan), ¹³CO (magenta), [O I], [C II] and [C I] (green), and HCO⁺ and HCN (black) lines labelled. The flux density scale is in Jy (assuming a point source).

emission (Visser et al. 2012; Yıldız et al. 2012). In NGC 1333 IRAS 4A/4B, however, the ¹²CO intensities and broad line-profiles of lower-*J* transitions (*J*=1-0 up to 10-9) probe swept-up or entrained shocked gas along the outflow (Yıldız et al. 2012).

In this paper we present the first complete far-IR and submm spectra of a Class 0 protostar (Serpens SMM1 or FIRS 1), taken with the PACS (Poglitsch et al. 2010) and SPIRE (Griffin et al. 2010) spectrometers on board the *Herschel Space Observatory* (Pilbratt et al. 2010). SMM1 is a low-mass proto-

stellar system located in the Serpens core (Eiroa et al. 2008) at a distance of $d=230\pm20$ pc (see also Dzib et al. 2010, for an alternative measurement). It is the most massive low-mass Class 0 source ($M_{\text{env}} \approx 16.1 M_{\odot}$, $T_{\text{bol}} \approx 39$ K) of the WISH program sample (*Water in Star-forming Regions with Herschel*, van Dishoeck et al. 2011). The *Herschel* spectra are complemented with mid-IR Spitzer Infrared Spectrograph (IRS) archive spectra of the embedded protostar (photometry first presented by Enoch et al. 2009).

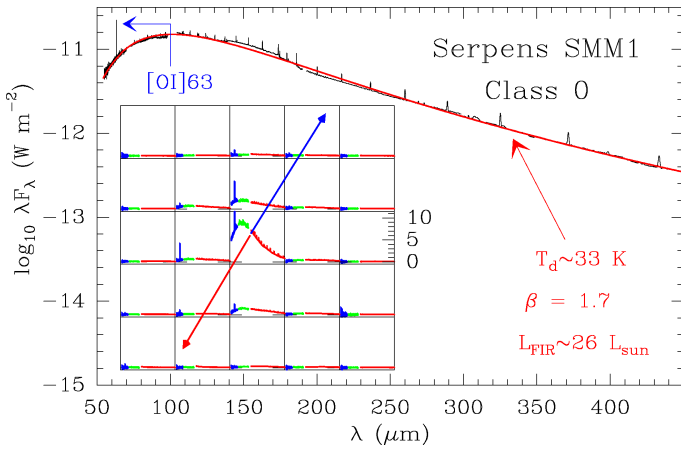


Fig. 2. Observed SED of Serpens SMM1 and modified black-body fit (red curve). Inset shows the full PACS array in flux density units of $10^{-14} \text{ W m}^{-2} \mu\text{m}^{-1}$. The abscissa is in linear scale from 55 to $190 \mu\text{m}$. The bright emission line seen in several positions is $[\text{O I}] 63 \mu\text{m}$. Approximate outflow directions are shown with red and blue arrows.

The Serpens cloud core was first mapped in the far-IR with the LWS spectrometer on board the *Infrared Space Observatory* (ISO). Even with a poor angular and spectral resolution of $\sim 80''$ and $R = \lambda/\Delta\lambda \sim 200$, ISO-LWS observations of Serpens SMM1 revealed a rich spectrum of molecular lines (Larsson et al. 2002), superposed onto a strong far-IR continuum (Larsson et al. 2000). In particular, ^{12}CO (up to $J=21-20$), H_2O (up to $4_{41}-3_{30}$) and some OH lines were detected. Detailed modeling of the ISO emission concluded that those species trace the inner $\sim 10^3 \text{ AU}$ regions around the protostar, where gas temperatures are above 300 K and densities above 10^6 cm^{-3} . The comparison of the H_2O , OH and CO lines with existing shock models suggested that shock heating along the SMM1 outflow is the most likely mechanism of molecular excitation. The details of these shocks, however, were less clear.

Because of its far-IR luminosity and rich spectrum, Serpens SMM1 is an ideal Class 0 source for studying the protostellar environment and to characterize the shock- and UV-heating and chemistry with the much higher spatial and spectral capabilities provided by *Herschel*. In the following sections we present the data set, we identify the observed lines, present a 3 component non-LTE radiative transfer model and compare the observations with available shock models and observations of other YSOs.

2. Observations and Data Reduction

2.1. Herschel PACS and SPIRE Observations

PACS spectra between ~ 55 and $\sim 210 \mu\text{m}$ were obtained on 31 October 2010 in the Range Spectroscopy mode. The PACS spectrometer uses photoconductor detectors and provides 25 spectra over a $47'' \times 47''$ field-of-view (FoV) resolved in 5×5 spatial pixels (“spaxels”), each with a size of $\sim 9.4''$ on the sky. The resolving power varies between $R \sim 1000$ (at $\sim 100 \mu\text{m}$ in the R1 grating order) and ~ 5000 (at $\sim 70 \mu\text{m}$ in the B3A order). The central spaxel was centered at the Serpens SMM1 protostar ($\alpha_{2000}: 18^{\text{h}}29^{\text{m}}49.8^{\text{s}}$, $\delta_{2000}: 1^{\circ}15'20.5''$). Observations were carried out in the “chop-nodded” mode with the largest chopper throw of 6 arcmin. The total observing time was $\sim 3 \text{ h}$ (observation IDs 1342207780 and 1342207781). The measured width

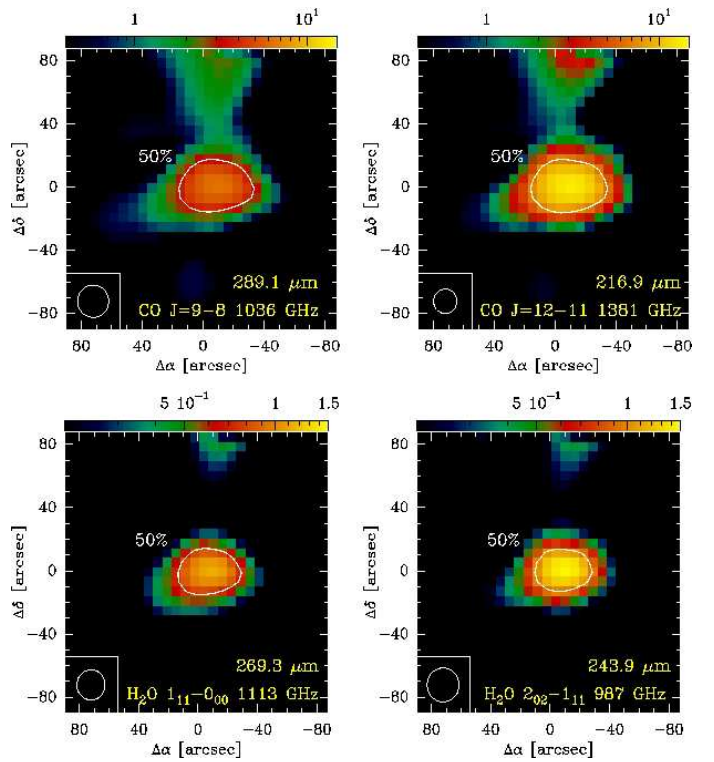


Fig. 3. Upper: SPIRE-FTS ^{12}CO $J=9-8$ and $12-11$ sparse maps. Lower: $p\text{-H}_2\text{O}$ $1_{11}-0_{00}$ and $2_{02}-1_{11}$ maps respectively. The line surface brightness is on the $10^{-8} \text{ W m}^{-2} \text{ sr}^{-1}$ scale. The white contours represent the 50% line emission peak level. The FWHM beam is shown in each inset. Note the increase of line surface brightness in the more excited lines.

of the spectrometer point spread function (PSF) is relatively constant for $\lambda \lesssim 100 \mu\text{m}$ (FWHM \approx spaxel size) but increases at longer wavelengths. In particular only $\approx 40\%$ ($\approx 70\%$) of a point source emission would fall in the central spaxel at $\approx 190 \mu\text{m}$ ($\lambda \approx 60 \mu\text{m}$). Hence, extracting line surface brightness from a semi-extended source like Serpens SMM1 is not trivial. In this work we followed the method described by Herczeg et al. (2012) and Karska et al. (submitted). This involves multiplying all line fluxes measured in the central spaxel with a λ -dependent *correction curve* calculated from the extended emission of the brightest CO and H_2O lines observed over the entire FoV. The correction factor is constant (~ 2) for $\lambda < 120 \mu\text{m}$ and increases from ~ 2 to $\sim 3-4$ at $\sim 200 \mu\text{m}$. For the continuum and $[\text{O I}]$ and $[\text{C II}]$ lines, the individual line fluxes measured in all spaxels were added. Note that we checked that the reference spectra in the two off positions are free of $[\text{C II}]$ emission to confirm that the $[\text{C II}]$ lines towards Serpens SMM1 are real. Figure 1 shows the PACS spectrum in the central spaxel and Fig. 2 shows the entire PACS array from 55 to $190 \mu\text{m}$ (the bright emission line is $[\text{O I}] 63 \mu\text{m}$).

SPIRE FTS spectra between ~ 194 and $\sim 671 \mu\text{m}$ (1545-447 GHz) were obtained on 27 March 2011. The SPIRE FTS uses two bolometer arrays covering the $194-313 \mu\text{m}$ (Short Wavelength array, SSW) and $303-671 \mu\text{m}$ (Long Wavelength array, SLW) bands. The two arrays contain 19 (SLW) and 37 (SSW) hexagonally packed detectors separated by ~ 2 beams ($51''$ and $33''$ respectively). The unvignetted FoV is $\sim 2'$. The observation was centered at Serpens SMM1 (IDs 1342216893) in the high spectral resolution mode ($\Delta\tilde{\lambda} = 0.04 \text{ cm}^{-1}$; $R \sim 500-1000$).

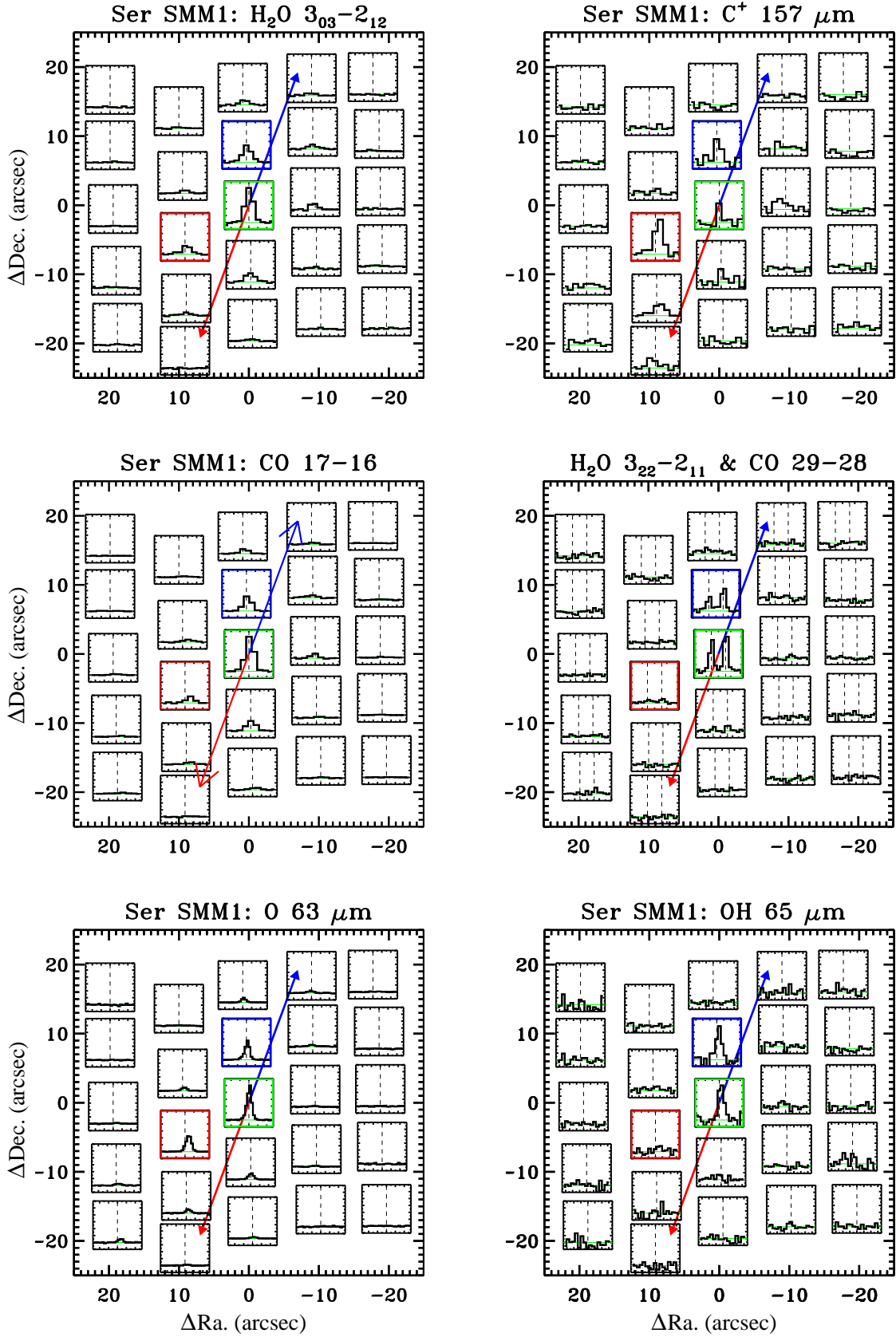


Fig. 4. PACS spectral maps of Serpens SMM1 in the o - $H_2O\ 3_{03}-2_{12}$ ($174.626\ \mu m$); $[C\text{II}]\ 157.741\ \mu m$; $CO\ J=17-16$ ($153.267\ \mu m$); both p - $H_2O\ 3_{22}-2_{11}$ ($89.988\ \mu m$) and $CO\ J=29-28$ ($90.163\ \mu m$); $[O\ I]63.183\ \mu m$ and $OH\ ^2\Pi_{3/2}\ J=9/2^+-7/2^-$ ($65.279\ \mu m$) lines (from top to bottom). The center of each spaxel corresponds to its offset position with respect to the protostar at $\alpha_{2000}: 18^h 29^m 49.8^s$, $\delta_{2000}: 1^{\circ}15'20.5''$. The Y-axis for each transition represents the normalized line flux (in the -0.2 to 1.2 range) with respect to the brightest line in the array. The X-axis represents the -550 to $550\ km\ s^{-1}$ velocity scale except for the $OH\ 65.279\ \mu m$ line (-350 to $350\ km\ s^{-1}$) and the p - $H_2O\ 89.988\ \mu m$ and $CO\ 90.163\ \mu m$ lines (-1000 to $1000\ km\ s^{-1}$). The vertical dashed lines show the position of the rest wavelengths. Blue and red arrows show the approximated outflow direction. The green box represents the central spaxel centered at the protostar position whereas the red and blue boxes represent postions in the red and blue outflow lobes respectively. Note that the PSF is relatively constant for $\lambda \lesssim 100\ \mu m$ ($FWHM \approx \text{spaxel size} \approx 9.4''$) but increases at longer wavelengths.

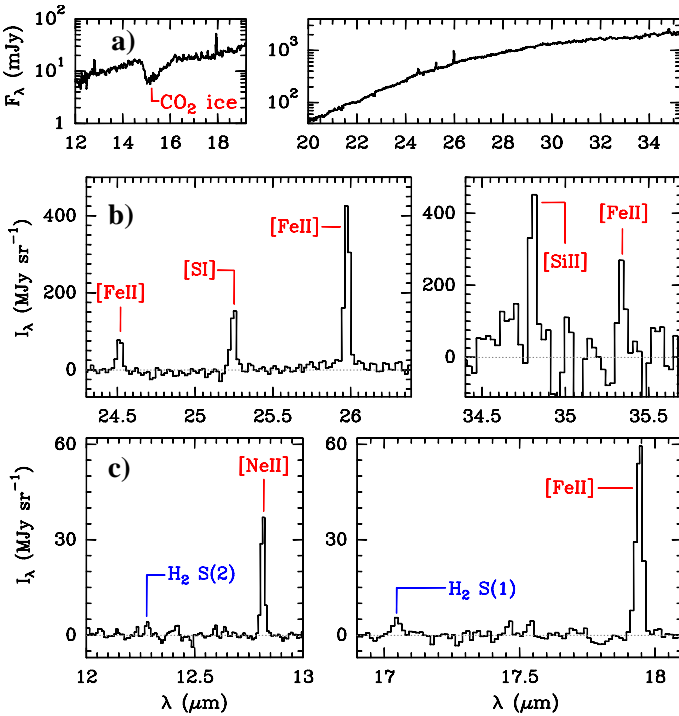


Fig. 5. (a) *Spitzer* IRS spectrum of the Class 0 protostar Serpens SMM1 using the Hi Res modules and a $7'' \times 7''$ aperture. (b) Continuum-subtracted spectra with main narrow lines identified in the LH module ($\lambda \geq 19.5\mu\text{m}$) and (c) with the SH module ($\lambda \leq 19.5\mu\text{m}$). Note the lack of bright molecular line emission (H_2O , OH , etc.).

The total integration time was ~ 9 min. We corrected the spectrum to account for the extended continuum and molecular emission of the source and the changing beam size with frequency across the SPIRE band. Taking account of the coupling of the source to the SPIRE-FTS beam (Wu et al. in prep.) and using the overlap region between the SSW and SLW bands as a reference (where the beam size differs by a factor of ~ 2) we calculate the FWHM size of the submm continuum source to be $\sim 20''$. The SPIRE continuum fluxes were appropriately corrected and the unapodized spectrum was used to fit the line intensities with sinc functions. Four representative mid- J ^{12}CO and H_2O integrated line intensity maps are shown in Figure 3.

SPIRE and PACS data were processed using HIPE and then exported to GILDAS where basic line spectrum manipulations were carried out. Tables A.1 and A.2 summarize the detected lines and the line fluxes towards the protostar position (central spaxel; corrected for extended emission in the case of PACS observations). The spatial distribution of several atomic and molecular lines observed in the PACS array is shown in Figure 4.

2.2. Spitzer IRS Observations

In order to complement the far-IR and submm *Herschel* spectra we have also analyzed mid-IR data towards the protostar position from the Infrared Spectrograph (IRS) on board *Spitzer* (Houck et al. 2004) in high spectral resolution mode ($R \sim 600$; 9.9 - $37.2\mu\text{m}$). The Basic Calibrated Data (BCD) files for the Short High (SH) and Long High (LH) orders of IRS were retrieved from the *Spitzer* Heritage Archive¹ (OBSID 34330, PI

M. Enoch). Pipelining of the data was achieved using CUBISM (Smith et al. 2007) to assemble the BCD files into spectral cubes. Bad and rogue pixels were removed using 3-sigma filtering. The spectra were extracted in a $\sim 7'' \times 7''$ aperture, thus close to the PACS spaxel size. The resulting *Spitzer* IRS spectra are shown in Figure 5. The photometry of these data was first presented by Enoch et al. (2009). Table A.3 summarizes the detected lines and their fluxes.

3. Results

3.1. Far-Infrared and Submillimeter Lines

Figure 1 shows the very rich PACS and SPIRE (lower panel) spectrum of the Serpens SMM1 protostar. More than 145 lines have been detected, most of them rotationally excited lines from abundant molecules: 38 ^{12}CO lines (up to $J=42$ -41 and $E_u/k=4971\text{K}$), 37 lines of both *o*- H_2O and *p*- H_2O (up to $8_{18}-7_{17}$ and $E_u/k=1036\text{K}$), 16 OH lines (up to $^2\Pi_{1/2}$ $J=7/2$ - $5/2$ and $E_u/k=618\text{K}$), 12 ^{13}CO lines (up to $J=16$ -15 and $E_u/k=719\text{K}$) and several HCN and HCO^+ lines (up to $J=12$ -11 and $E_u/k=283\text{K}$). Weaker $[\text{CII}]158\mu\text{m}$ and $[\text{CI}]370$, $609\mu\text{m}$ lines are also detected. Excited lines from NH_3 , CH^+ , CO^+ , OH^+ or H_2O^+ are however not detected at the PACS and SPIRE spectral resolutions and sensitivity. The brightest line in the spectra is the $[\text{OI}]63\mu\text{m}$ line (see also Figure 2) with a luminosity of $L_{63} \approx 0.014 L_\odot$. Assuming no extinction in the far-IR, we measure $[\text{OI}]63\mu\text{m}/[\text{CII}]158\mu\text{m} \approx 30$ and $[\text{OI}]63\mu\text{m}/[\text{OI}]145\mu\text{m} \approx 10$ line flux ratios integrated over the entire PACS array.

Most of the far-IR continuum and line emission arises from the protostar position (central spaxel) with weaker, but detectable, contributions from adjacent outflow positions (see Figure 4). In particular, the high excitation lines of CO, H_2O and OH detected below $\lambda < 100\mu\text{m}$ seem to show a more compact distribution than the lower excitation lines (within the PACS PSF sampling caveats). The highest PACS spectral resolution (~ 90 - 60 km s^{-1}) is achieved in the ~ 60 - $70\mu\text{m}$ range. Although at this resolution all detected molecular lines are spectrally unresolved (they have narrower intrinsic line-widths), the observed $[\text{OI}]63\mu\text{m}$ line is $>30\%$ broader than any close-by molecular line in the ~ 60 - $70\mu\text{m}$ range. This likely indicates that PACS marginally resolves the $[\text{OI}]63\mu\text{m}$ line, being broader (or having higher velocity line-wing emission) than the excited far-IR CO, H_2O and OH lines. In addition, the $[\text{OI}]63\mu\text{m}$ line-profile peak shifts in velocity from the protostar position (where the line is brightest) to the outflow red-lobe position where the line peak is redshifted by $\sim 100\text{ km s}^{-1}$ (more than a resolution element) and the molecular line emission is weaker (see red boxes in Figure 4). Note that $[\text{CII}]158\mu\text{m}$ peaks at this red-lobe position and the line peak is also redshifted by $\sim 100\text{ km s}^{-1}$ (although less than a resolution element in this wavelength range). Similar $[\text{OI}]63\mu\text{m}$ velocity-shifts are also seen in sources such as HH46 and are associated with the emission from an atomic jet itself (van Kempen et al. 2010). We refer to Karska et al. (submitted) for a detailed comparison of the $[\text{OI}]63\mu\text{m}$ shifts in several outflows.

Finally, the lower energy submm lines, from ^{12}CO and H_2O in particular, show a more extended distribution than the far-IR lines, with some indication of outflow emission in the the S-E direction (see SPIRE maps in Figure 3).

Table 1 summarizes the total line luminosities adding all observed lines between ~ 55 and $671\mu\text{m}$. Note that a few unidentified lines (U) are present in the PACS spectrum.

¹ <http://sha.ipac.caltech.edu/applications/Spitzer/SHA/>

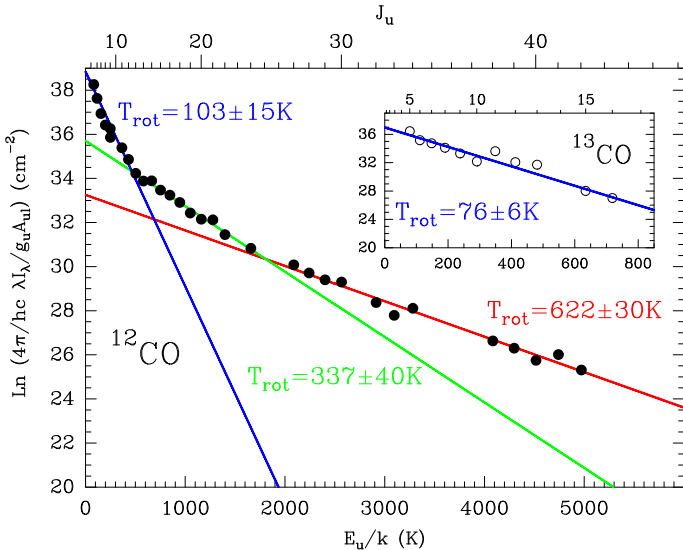


Fig. 6. ^{12}CO and ^{13}CO rotational diagrams obtained from PACS and SPIRE spectra. The estimated error in T_{rot} for ^{12}CO corresponds to different choices of J_u cutoffs for the different components. The range of possible T_{rot} for ^{13}CO reflects the standard error on the fitted values.

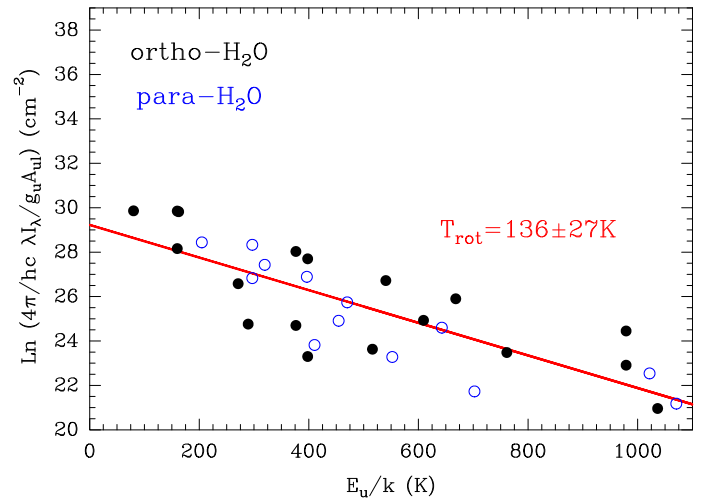


Fig. 7. H_2O rotational diagram showing $o\text{-H}_2\text{O}$ (filled circles) and $p\text{-H}_2\text{O}$ far-IR lines (open circles). Owing to subthermal excitation ($T_{\text{rot}} \ll T_k$) and large opacities of most lines, the H_2O diagram displays a larger scatter (standard error on the fitted values are shown) than CO.

3.2. Mid-Infrared Lines and Extinction

The mid-IR spectrum of Serpens SMM1 (Figure 5a) shows a much less rich spectrum than in the far-IR domain (probably due to severe dust extinction and lack of spectral resolution). Nevertheless, two weak H_2 pure rotational lines (0-0 $S(1)$ and $S(2)$ transitions) and seven brighter atomic fine-structure lines of Ne^+ , Si^+ , S and Fe^+ (four transitions) are clearly detected² at the protostellar position (Figures 5b and 5c). In contrast with NGC 1333-IRAS 4B (Watson et al. 2007), no mid-IR OH and H_2O lines are seen. The presence of $[\text{Ne II}]$ and $[\text{Fe II}]$ lines from energy levels above a few thousands Kelvin, together with the bright and velocity-shifted $[\text{O I}]$ line detected by *Herschel*, suggests the presence of fast dissociative shocks close to the protostar (e.g., Hollenbach & McKee 1989; Neufeld & Dalgarno 1989). Note that the same mid-IR lines are readily detected in Herbig-Haro objects and outflow lobes (e.g., Neufeld et al. 2006; Melnick et al. 2008). As discussed in Sect. 4, the observed intensities of H_2 , H_2O and CO rotational lines are more typical of slower velocity shocks.

The large amount of gas and dust in embedded YSOs requires to apply extinction corrections to retrieve corrected mid-IR line luminosities. In this work we have taken grain optical properties from Laor & Draine (Laor & Draine 1993) and computed an extinction curve $A(\lambda)/A_V$ from IR to submm wavelengths characterized by $R_V = A_V/E(B-V) = 5.5$ (the ratio of visual extinction to reddening) and a conversion factor from extinction to hydrogen column density of $1.4 \times 10^{21} \text{ cm}^{-2} \text{ mag}^{-1}$. These values have been previously used to correct photometric observations of embedded YSOs in the Serpens cloud (Evans et al. 2009). Table 1 lists the uncorrected mid-IR line luminosities and those using an arbitrary correction of $A_V = 150$. In the latter case, even the $[\text{O I}]63 \mu\text{m}$ line would be affected by extinction (the de-reddened line flux would be ~ 2 times higher) and the $[\text{O I}]63/145 \mu\text{m}$ line flux ratio would increase to ~ 20 .

² First ionization potential of observed ionic species are: 21.56 (Ne), 11.26 (C), 10.36 (S), 8.15 (Si) and 7.90 eV (Fe).

Such large intensity ratios are predicted by dissociative shocks models (e.g., Hollenbach & McKee 1989; Neufeld & Dalgarno 1989; Flower & Pineau Des Forets 2010) and thus provide a reasonable upper value to the extinction in the inner envelope. An independent estimate of the extinction is obtained from the $\sim 9.7 \mu\text{m}$ silicate grains absorption band seen in the *Spitzer* IRS low resolution spectra (shown in Enoch et al. 2009). In the diffuse ISM, the optical depth of the $\sim 9.7 \mu\text{m}$ broad feature is proportional to A_V (e.g., Whittet 2003). Although it is not clear that the same correlation holds in the dense protostellar medium (Chiar et al. 2007), we computed a lower limit to the extinction of $A_V \gtrsim 30$ by fitting the $\sim 9.7 \mu\text{m}$ absorption band and assuming a single slab geometry.

3.3. Dust Continuum Emission

The dust continuum emission peaks in the far-IR domain at $\sim 100 \mu\text{m}$. This is consistent with the presence of a massive dusty envelope with relatively warm dust temperatures. Using a simple modified blackbody with a dust opacity varying as $\tau_\lambda = \tau_{100}(100/\lambda)^\beta$, where τ_{100} is the continuum opacity at $100 \mu\text{m}$ and β is the dust spectral index, we obtain a size of $\sim 7''$ for the optically thick far-IR continuum source, with $\tau_{100} \approx 2.5$, $\beta = 1.7$, $L_{\text{far-IR}} \approx 26 L_\odot$ and a dust temperature of $T_d \approx 33 \text{ K}$ (Fig. 2). These parameters agree with more sophisticated radiative transfer models of the continuum emission detected with ISO/LWS, for which a far-IR source size of $\sim 4''$ ($\sim 500 \text{ AU}$ in radius) and $T_d = 43 \text{ K}$ at the $\tau_{100}=1$ equivalent radius were inferred (Larsson et al. 2000). They are also consistent with more recent SED models (Kristensen et al. 2012) and with the compact ($\sim 5''$) emission revealed by mm interferometric observations and thought to arise from the densest regions of the inner envelope and from outflow material (Hogerheijde et al. 1999; Enoch et al. 2009). Note that owing to the large continuum opacity below $100 \mu\text{m}$, observations at these wavelengths probably do not trace the innermost regions, i.e., the developing cir-

Table 1. Observed and modelled luminosities.

Species	$\log_{10} L_{\text{obs}} (L_{\odot})$	% ^a	% of L_{obs} in each component ^b
¹² CO	-1.17	54%	~15% (<i>h</i>) ~60% (<i>w</i>) ~25% (<i>c</i>)
H ₂ O	-1.56	22%	~90% (<i>h</i>) ~10% (<i>c</i>)
[O I]	-1.82	12%	~100% (<i>w</i>)
OH	-1.94	9%	~100% (<i>w</i>)
¹³ CO	-2.75	1%	~40% (<i>w</i>) ~60% (<i>c</i>)
[C II]	-3.32	0%	~100% (<i>w</i>)
[C I]	-3.42	0%	~10% (<i>w</i>) ~90% (<i>c</i>)
Dust	1.41	-	
H ₂	-(4.83-2.54 [†])		
[Fe II]	-(3.57-2.62 [†])		
[Si II]	-(3.98-2.03 [†])		
[S I]	-(4.52-3.07 [†])		
[Ne II]	-(4.93-2.67 [†])		

^(a) Fraction of total far-IR/submm line luminosity.^(b) From simple model: *h*=hot, *w*=warm, *c*=cool component.^(†) From *Spitzer* IRS observations (10-37 μm). Upper limits include an arbitrary extinction correction of $A_V=150$ mag.

cumstellar disk with an approximate radius of ~ 100 AU (*e.g.*, Rodríguez et al. 2005).

4. Analysis

4.1. ¹²CO, ¹³CO, H₂O and OH Rotational Ladders

Figure 6 shows all ¹²CO and ¹³CO detected lines in a *rotational diagram*. In this plot we assumed that the line emission arises from a source with a radius of 500 AU (see Sect. 3.3). Given the high densities in the inner envelope of protostars ($>10^6 \text{ cm}^{-3}$; see below), the rotational temperatures (T_{rot}) derived from these plots are a good lower limit to T_k . The ¹²CO diagram suggests the presence of 3 different T_{rot} components with $T_{\text{rot}}=622\pm30$ K (for $J_u\lesssim42$), $T_{\text{rot}}=337\pm40$ K ($J_u\lesssim26$) and $T_{\text{rot}}=103\pm15$ K ($J_u\lesssim14$) respectively. The estimated error in T_{rot} corresponds to different choices of J_u cutoffs for the different components³. In the following we shall refer to them as the *hot*, *warm* and *cool* components. Whether or not these T_{rot} components are associated with 3 real physical components or with a more continuous temperature and mass distribution will be discussed in Section 4.1. Here we note that the submm low-*J* CO emission shows broad line-profiles and a more extended distribution (Davis et al. 1999; Dionatos et al. 2010) than the high-*J* CO and H₂O lines detected with PACS (more sharply peaked near the protostar). In addition, velocity-resolved observations with HIFI of high-*J* CO lines up to $J=16-15$ show different profiles compared with low-*J* CO lines (Yıldız et al. 2012, Kristensen et al., in prep.). Specifically, for the ¹²CO $J=10-9$ profile toward SMM1, Yıldız et al. (in prep.) find that about 1/3 of the integrated intensity is due to a narrow (FWHM of a few km s^{-1}) component originating from the quiescent envelope and 2/3 to the broad outflow component. Thus, the cool gas component seen in the SPIRE submm maps is dominated by the entrained outflow gas. On the other hand, the CO $J=16-15$ profile of SMM1 is less broad and more similar to the excited H₂O line profiles observed with HIFI (Kristensen et al., in prep.). Thus, the far-IR CO and H₂O lines detected by PACS clearly probe different physical components than the SPIRE data.

³ Note that an extinction correction of $A_V=150$ will only imply slightly larger far-IR line fluxes (more than a factor 1.5 below $\sim 80 \mu\text{m}$). Slightly higher rotational temperatures would be inferred if $A_V=150$ (~ 350 K and ~ 700 K for the *warm* and *hot* components respectively).

Alternatively, Neufeld (2012) pointed out that the shape of the rotational diagrams do not, by themselves, necessarily require multiple temperature components. In particular, a single- T_{rot} solution could be found for the ¹²CO $J_u>14$ lines in Serpens SMM1 if the gas were very hot ($T_{\text{kin}}\simeq 2500$ K) but had a low density (a few 10^4 cm^{-3}). This scenario seems less likely, at least for the circumstellar gas in the vicinity of the protostar. Note that the gas density in the inner envelope of SMM1 is necessarily higher, as probed by our detection of high-*J* lines from high dipole moment molecules such as HCN and HCO⁺ (with very high critical densities). In addition, detailed SED models predict densities of $n(\text{H}_2)\simeq 4\times 10^6 \text{ cm}^{-3}$ at ~ 1000 AU, whereas densities of the order of $\sim 10^5 \text{ cm}^{-3}$ are only expected at much larger radii (Kristensen et al. 2012). Therefore, it seems more likely that the different T_{rot} slopes probe different physical components or the presence of a temperature gradient.

A rotational diagram of the detected ¹³CO lines provides $T_{\text{rot}}=76\pm6$ K, thus lower than the T_{rot} inferred for ¹²CO in the *cool* component. The measured ¹²CO/¹³CO $J=5-4$ line intensity ratio is $\simeq 8$, thus much lower than the typical ¹²C/¹³C isotopic ratio of ~ 60 Langer & Penzias (1990), whereas the ¹²CO/¹³CO $J=16-15$ intensity ratio is $\simeq 55$. These different ratios show that the submm ¹²CO low- and mid-*J* lines are optically thick, but the high-*J* far-IR lines are optically thin.

An equivalent plot of the observed far-IR H₂O line intensities in a rotational diagram gives $T_{\text{rot}}=136\pm27$ K without much indication of multiple T_{rot} components (Figure 7). Since H₂O critical densities are much higher than those of CO, collisional thermalization only occurs at very high densities ($>10^8 \text{ cm}^{-3}$). Therefore, the large scatter of the H₂O rotational diagram is a consequence of subthermal excitation conditions ($T_{\text{rot}}\ll T_k$) and large H₂O line opacities. We anticipate here that the opacity of most (but not all) far-IR H₂O lines is very high ($\tau\gg 1$). Compared to CO, the H₂O rotational diagram is thus obviously less meaningful. A similar rotational diagram of the observed OH lines provides $T_{\text{rot}}=72\pm8$ K (see also Wampfler et al., submitted), even lower than the inferred H₂O rotational temperature. Like H₂O, OH transitions also have high critical densities and line opacities (except the high-energy and the cross-ladder transitions).

4.2. Simple Model of the Far-IR and Submm Line Emission

Observations and models of the protostellar environment suggest that the observed emission can arise from different physical components, where different mechanisms dominate the gas heating and the prevailing chemistry: hot and warm gas from energetic shocks in the inner envelope (*e.g.*, small scale shocks along the outflow cavity walls, bow shocks and working surfaces within an atomic jet); UV-illuminated gas in the cavity walls; cooler gas from the envelope passively heated by the protostar luminosity and the entrained outflow gas (*e.g.*, van Dishoeck et al. 2011). Unfortunately, the lack of enough spectral and angular resolution of our data does not allow us to provide a complete characterization of all the different possible components. However, the large number of detected lines, high excitation ($E_u/k>300$ K) optically thin lines in particular, helps to determine the dominant contributions and the average physical conditions.

With this purpose, we have carried out a non-LTE radiative transfer model of the central spaxel far-IR and submm spectrum (the protostar position) using a multi-molecule LVG code (Cernicharo 2012). In this model we included three spherical components suggested by the three temperature components seen in the ¹²CO rotational diagram (*i.e.*, *hot*, *warm* and *cool* components). In our model, CO is present in the three compo-

Table 2. Model components and source-averaged column densities (assuming a line-width of 20 km s⁻¹ in all components).

Comp.	Radius	T_k (K)	$n(\text{H}_2)$ (cm ⁻³)
<i>Hot</i>	~500 AU	800	5×10^6
$N(\text{cm}^{-2})$	$^{12}\text{CO}(5 \times 10^{16})$ $^{13}\text{CO}(9 \times 10^{14})$	$\text{H}_2\text{O}(2 \times 10^{10})$	
<i>Warm</i>	~500 AU	375	5×10^6
$N(\text{cm}^{-2})$	$^{12}\text{CO}(1 \times 10^{18})$ OH(1×10^{16}) HCN(2×10^{14}) CO+(<2 $\times 10^{15}$) O(1×10^{18})	$^{13}\text{CO}(2 \times 10^{16})$ $\text{HCO}^+(5 \times 10^{14})$ $\text{CH}^+(<2 \times 10^{14})$ $\text{NH}_3(<2 \times 10^{15})$	
<i>Cool</i>	~4500 AU	140	2×10^5
$N(\text{cm}^{-2})$	$^{12}\text{CO}(1 \times 10^{17})$ $^{13}\text{CO}(1 \times 10^{16})$ HCN(1×10^{15}) C+(&mathgt10^{16})	$\text{H}_2\text{O}(8 \times 10^{15})$ $\text{HCO}^+(2 \times 10^{14})$ $\text{C}(1 \times 10^{17})$	

ments, but since a single rotational temperature roughly explains the observed far-IR H₂O and OH lines, most of their emission in the PACS domain can be reproduced with only one component, the *hot* component for H₂O and the *warm* component for OH (see next section for more details). Note that we do not model the extended quiescent envelope with the bulk of the (cold) mass seen in the mm continuum and narrow C¹⁸O line emission (Yıldız et al. in prep.). Foreground absorption and emission from the low density and low temperature extended envelope are thus not included in the model but they will basically influence narrow velocity ranges of the lowest energy-level lines.

The latest available collisional rates were used (*e.g.*, Daniel et al. 2011 and references therein for H₂O and Yang et al. 2010, extended by Neufeld 2012, for CO). Although only one line of *o*-H₂ and one line of *p*-H₂ are detected towards the Serpens SMM1 protostar position, the large H₂ 0-0 *S*(2)/*S*(1) line intensity ratio suggests a H₂ *ortho*-to-*para* (OTP) ratio lower than 3 in the gas probed by these low excitation H₂ lines. Here we shall adopt an OTP ratio for H₂ of 1 (the value we obtain from the two observed H₂ lines assuming LTE and a rotational temperature of ~800 K). Note that such low non-equilibrium H₂ OTP values have been inferred, for example, in the hot shocked gas towards HH54 and HH7-11 (Neufeld et al. 2006). The water vapour OTP ratio in the model, however, is let as a free parameter.

The *o*-H₂O ground-state line observed with HIFI towards Serpens SMM1 shows a two component emission line profile with a *medium* component ($\Delta v \approx 15 \text{ km s}^{-1}$) thought to arise from small-scale shocks in the inner cavity walls and a *broad* component ($\Delta v \approx 40 \text{ km s}^{-1}$) from more extended shocked-gas along the outflow (Kristensen et al. 2012). In addition, velocity-resolved observations of the OH $^2\Pi_{1/2}$ $J=3/2-1/2$ line (~163.1 μm) with HIFI show a broad line-profile with $\Delta v \approx 20 \text{ km s}^{-1}$ (Wampfler, S. priv. comm.). For simplicity here we shall adopt a typical line-width of 20 km s⁻¹ in all modelled components. As in any LVG calculation, the model is more accurate for (effectively) optically thin lines (high-*J* CO lines, excited and weak H₂O and OH lines, etc.) than for very opaque lines (*e.g.*, low excitation lines).

4.2.1. Model: Hot and Warm Component

Following Sect. 3.3. and previous far-IR studies of this source, we have assumed a size of ~4'' (~500 AU in radius; *e.g.*, Larsson et al. 2000; Kristensen et al. 2012) for the far-IR source (*hot* and *warm* components), a mixture of shocked and UV-illuminated gas (see Section 5). A good fit to the high-*J* ^{12}CO

emission is obtained for $n(\text{H}_2) \approx 5 \times 10^6 \text{ cm}^{-3}$ with $T_k \approx 800 \text{ K}$ and $\approx 375 \text{ K}$ for the *hot* and *warm* components respectively. The approximate mass in these components is only $M \lesssim 0.03 M_\odot$. Although this solution is not unique, this model satisfactorily reproduces not only the ^{12}CO high-*J* lines but also the lines from other species (note that we searched for a combination of T_k and $n(\text{H}_2)$ that reproduces all species simultaneously; see below).

In order to constrain the density and place H₂O and OH in a particular model component, we first run a grid of excitation models and investigated how particular line ratios change with $n(\text{H}_2)$ and T_k . In this comparison we choose faint, low-opacity lines arising from high energy levels that are observed with a similar PSF. Figure A.1 shows the variation of the *o*-H₂O $3_{30}-3_{03}/6_{15}-3_{05}$ (67.269/82.031 μm) and *p*-H₂O $6_{06}-5_{15}/5_{15}-4_{04}$ (83.284/95.627 μm) line ratios. The former ratio shows that the excited H₂O lines arise from dense gas, whereas the latter requires high temperatures (>500 K). The intersection of the two line ratios is consistent with densities higher than a few 10^6 cm^{-3} and temperatures around ~800 K. Note that for $T_k < 400 \text{ K}$, the predicted emission from many excited H₂O lines below ~100 μm would be too faint. On the other hand, Figure A.2 shows a very clear dependence of the OH 65.279/96.363 μm line ratio with the gas temperature. The observed ratio does suggest that OH arises from gas at $T_k \lesssim 400 \text{ K}$. Following the previous excitation analysis, and according to the higher observed rotational temperatures ($T_{\text{rot}}^{\text{H}_2\text{O}} > T_{\text{rot}}^{\text{OH}}$) and higher H₂O energy levels detected, we placed H₂O in the *hot* component and OH (together with [OI]) in the *warm* component. Although this choice provides a better fit to the data, we can not obviously conclude that the bulk of the water vapour and OH emission arise from different physical components.

Far-IR radiative pumping is not included in our models and thus the derived H₂O and OH column densities might be considered as upper limits. Nevertheless, all H₂O and OH lines are observed in emission and show $T_{\text{rot}} > T_d$ (where T_d is the dust temperature inferred from the SED analysis, see Sect. 3.3), suggesting that owing to the high densities but moderate far-IR radiation field at $\gtrsim 500 \text{ AU}$, collisions dominate at first order. Note that high-mass protostars produce much stronger far-IR dust continuum fields (by orders of magnitude) and many far-IR OH and water vapour lines are often observed in absorption or show P-Cygni profiles when far-IR pumping dominates the excitation (see *e.g.*, Goicoechea et al. 2006; Cernicharo et al. 2006, for far-IR OH and H₂O lines in Orion KL outflows).

4.2.2. Model: Cool Gas Component

In order to fit the more extended ^{12}CO low- and mid-*J* emission and to match the $T_{\text{rot}} \approx 100 \text{ K}$ component seen in the ^{12}CO rotational diagram (Figure 6), we included a third *cool* component – the entrained outflow gas. From the SPIRE ^{12}CO maps we infer an approximate radius of ~20'' (~4500 AU) for the emitting region. For this geometry, a density of $n(\text{H}_2) \approx 2 \times 10^5 \text{ cm}^{-3}$ and a temperature of $T_k \approx 140 \text{ K}$ produces a good fit of the observed ^{12}CO submm emission (see also Yıldız et al. 2012, for velocity-resolved observations in NGC 1333 IRAS 4A/4B). This component is also needed to fit the lower excitation H₂O submm lines.

Low- and mid-*J* ^{13}CO lines are optically thin and thus, in addition to the swept-up or entrained outflow gas, velocity-resolved submm ^{13}CO line profiles would carry information about other components such as the UV-heated gas and the quiescent envelope, which may well dominate the ^{13}CO lower-*J* emission (Yıldız et al. 2012). Detailed models of the emission

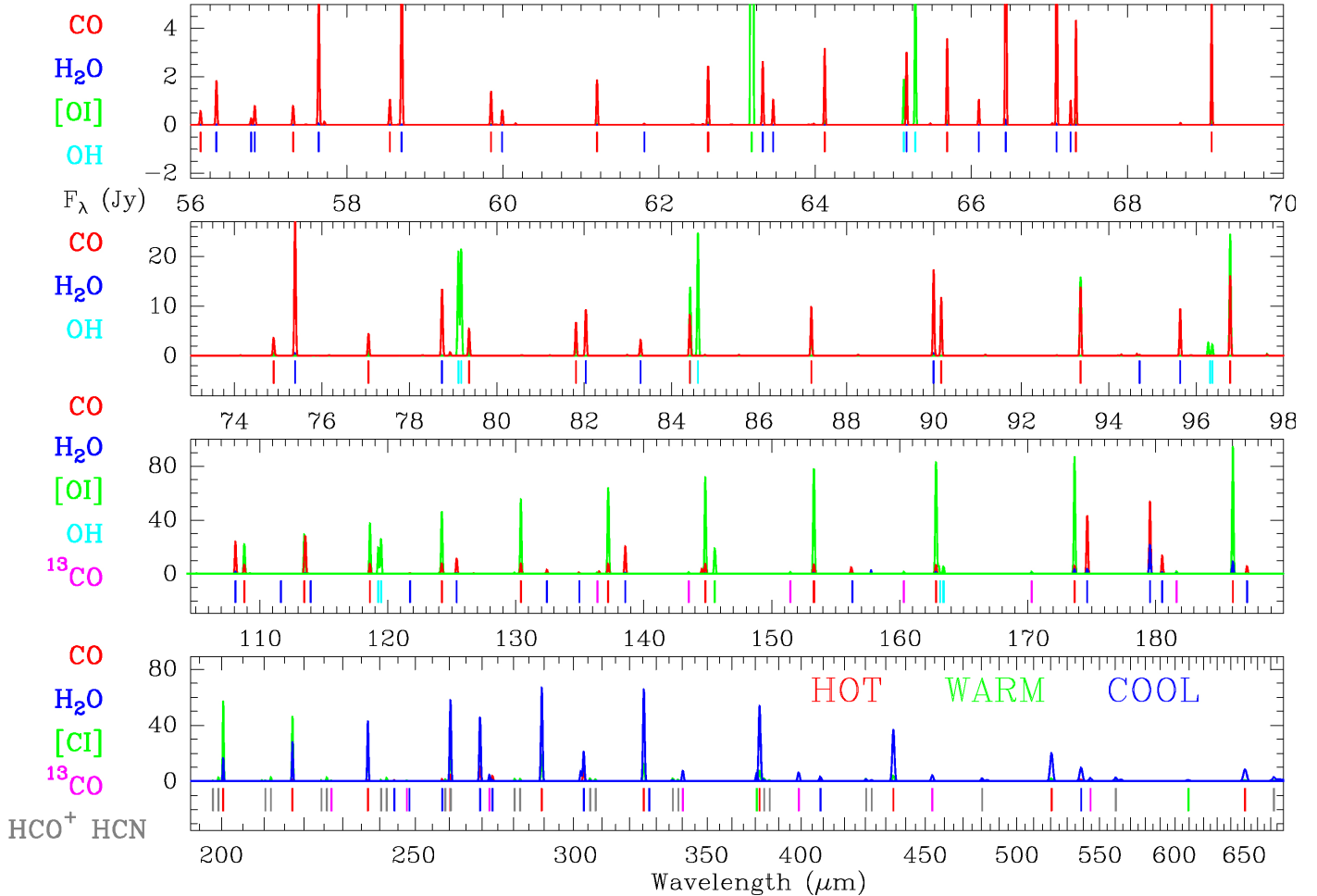


Fig. 8. Synthetic non-LTE LVG spectrum of the Class 0 protostar Serpens MM1 convolved to PACS (top three panels) and SPIRE (lower panel) spectral resolutions. Continuous curves show the line emission contribution from the “hot” (red), “warm” (green) and “cool” (blue) components discussed in the text. Vertical labels mark the wavelength position of CO (red), H₂O (blue), OH (cyan), ¹³CO (magenta), HCO⁺ and HCN (grey) rotational transitions. [O I]63, 145 and [C I]370, 609 μm fine structure lines are marked with green labels.

from the extended and passively heated envelope (having most of the mass) predict ¹²CO rotational temperatures around ≈ 30 –60 K (Visser et al. 2012, Harsono et al., in prep).

To summarize, Table 2 shows the model parameters and Figure 8 shows the entire ~ 55 to $671\mu\text{m}$ synthetic spectrum for the *hot* (red), *warm* (green) and *cool* (blue) components convolved with the PACS and SPIRE resolutions. A comparison of the resultant synthetic spectrum (by simply adding the 3 component spectra) with the *Herschel* spectra is shown in Figure 9.

4.2.3. Columns, Abundances and Validity of the Model

Owing to the lack of angular resolution to determine the beam filling factors of the different physical components towards Serpens SMM1, the relative abundance ratios derived from the model and shown in Table 3 are a better diagnostic tool than the absolute column densities. Nevertheless, here we provide the source-averaged column densities (N) in the different components as well as the upper limits for several non-detected species (Table 2). In the *hot* component we find $\sim 5 \times 10^{16}\text{ cm}^{-2}$ and $\sim 2 \times 10^{16}\text{ cm}^{-2}$ column densities for ¹²CO and H₂O respectively. Note that a water vapour OTP ratio of ~ 3 provides the best fit

to the observed water vapour lines and this is the value adopted in the models. Assuming that the gas in the *warm* component ($T_k \approx 375$ K) covers a similar area, we obtain $N(\text{OH}) \sim 10^{16}\text{ cm}^{-2}$ and $N(^{12}\text{CO}) \sim 10^{18}\text{ cm}^{-2}$ (a factor ≈ 20 larger than $N(^{12}\text{CO})$ in the *hot* component).

The detected mid-IR H₂ lines provide a lower limit to the H₂ column density of $N_{\text{H}_2} \approx 10^{22}\text{ cm}^{-2}$. We use this column density to provide an upper limit to the absolute abundances (with respect to H₂) in the *hot+warm* components. In particular we obtain $\lesssim 10^{-4}$, $\lesssim 0.2 \times 10^{-5}$ and $\lesssim 10^{-6}$ for the CO, H₂O and OH abundances respectively. The inferred upper limit to the water vapour abundance is much higher than the $\approx 10^{-(8-9)}$ value typically found in cold interstellar clouds (e.g., Caselli et al. 2010) but is lower than the $\approx 10^{-4}$ value often expected in the hot shocked gas (e.g., Kaufman & Neufeld 1996). Note that the high source-averaged column density of atomic oxygen ($\sim 10^{18}\text{ cm}^{-2}$) suggests that a significant fraction of gas-phase oxygen reservoir in shocks is kept in atomic form.

The column densities in the entrained outflow gas (*cool* component at $T_k \approx 140$ K) are given in Table 2. The absolute columns are more uncertain as they depend on the assumed spatial distribution of the swept-up outflow gas. Note that in order to fit

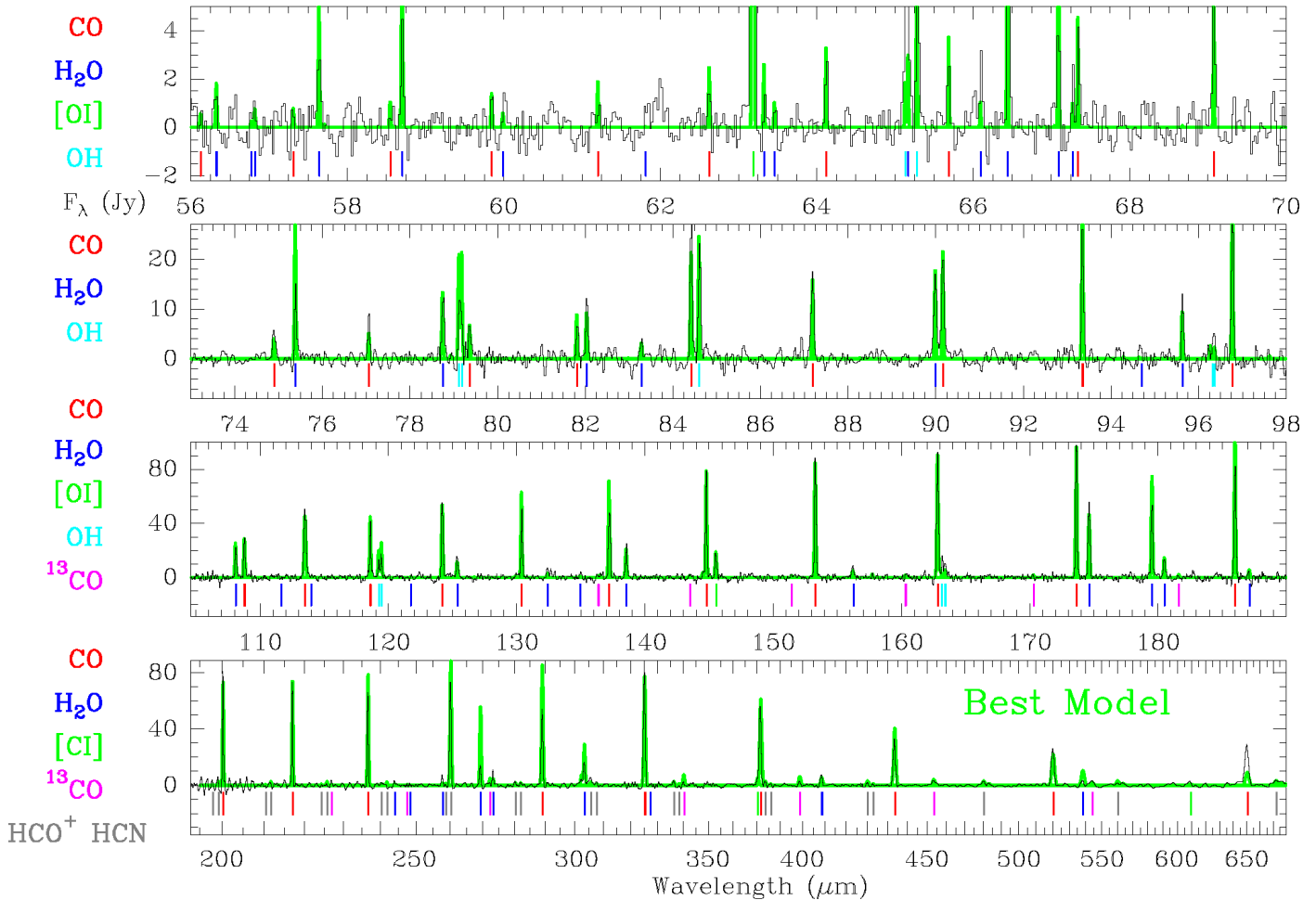


Fig. 9. *Herschel* far-IR and submm spectrum of Serpens SMM1 at the central spaxel position (black histogram) and complete model (green continuous curves) adding the emission from the *hot*, *warm* and *cool* components and convolved to PACS and SPIRE spectral resolutions.

Table 3. Selected abundance ratios in the modelled components.

Species	Abundance ratio	Component
$\text{H}_2\text{O}_h/(\text{CO}_w + \text{CO}_h)$	~0.02	<i>hot</i> and <i>warm</i>
$\text{OH}_w/(\text{CO}_w + \text{CO}_h)$	~0.01	<i>hot</i> and <i>warm</i>
$\text{O}_w/(\text{CO}_w + \text{CO}_h)$	~0.8	<i>hot</i> and <i>warm</i>
$\text{OH}_w/\text{H}_2\text{O}_h$	$\lesssim 0.5$	<i>warm/hot</i>
CO_w/CO_h	~20	<i>warm/hot</i>
$\text{H}_2\text{O}_h/\text{CO}_h$	~0.4	<i>hot</i>
$\text{CH}_h^+/\text{H}_2\text{O}_h$	<0.01	<i>hot</i>
O_w/OH_w	~100	<i>warm</i>
$\text{HCO}_w^+/\text{HCN}_w$	~2.5	<i>warm</i>
$\text{HCO}_c^+/\text{HCN}_c$	~0.2	<i>cool</i>
$\text{H}_2\text{O}_c/\text{CO}_c$	<0.08	<i>cool</i>

the low- J ^{13}CO lines in the *cool* component, we had to include a low $^{12}\text{CO}/^{13}\text{CO}$ column density ratio of ≈ 10 , confirming that the low- J ^{12}CO lines are optically thick and thus they do not probe the bulk of the material seen in the low- J CO isotopologue line emission (*i.e.*, the massive and quiescent envelope).

Our simple LVG model satisfactorily reproduces the absolute fluxes of most observed lines and does not predict lines that are not detected in the spectra (see Figure 9). Despite the fact that this model solution is obviously not unique, the agreement

with observations suggests that this model captures the average physical conditions of the shocked gas near the protostar. The level of agreement is typically better than $\sim 30\%$ (*i.e.*, similar to the calibration uncertainty). The worst agreement occurs for several low-excitation optically thick lines that can arise from different physical components because the non-local radiative coupling between different components is not treated in the LVG model. In addition, some lines such as the $\sim 163\mu\text{m}$ OH lines (sensitive to far-IR pumping, see Offer & van Dishoeck 1992; Goicoechea & Cernicharo 2002) are underestimated by $\gtrsim 40\%$, suggesting that radiative pumping may play some role (see detailed OH models by Wampfler et al., submitted).

Regarding the T_k and $n(\text{H}_2)$ conditions inferred in each component, Figure A.3 in the Appendix shows that for a given gas density, we can distinguish temperature variations of $\sim 30\%$ (especially in high- J CO and in some high excitation H_2O and OH lines). Figure A.4 shows that for a given gas temperature, density variations of a factor $\sim 2\text{-}3$ can also be distinguished. Therefore, for the assumed geometry and physical conditions, the derived source-averaged column densities are accurate within a factor of ~ 2 .

5. Discussion

5.1. Shocked-Gas Components

Several fine-structure lines that probe the very hot atomic gas (a few thousand K) near the protostar are detected in the mid-IR. Besides, most tracers of the shock-heated molecular gas (a few hundred K) appear in the far-IR. At longer submm and mm wavelengths, extended emission from cool entrained outflow gas and from the cold massive envelope dominates. The relative intensities of the detected mid- and far-IR atomic and molecular lines help to qualitatively constrain the nature of the main shocked-gas components in Serpens SMM1.

The shock wave velocity, pre-shock density and the magnetic field strength determine most of the shocked gas properties. Fast shocks can destroy molecules and ionize atoms, whereas slower shocks heat the gas without destroying molecules. Depending on the evolution of the shock structure it is common to distinguish between *J*-type (or Jump) and *C*-type (or Continuous). More complicated, “mixed” non-stationary situations may also exist (see reviews by *e.g.*, Draine & McKee 1993; Walmsley et al. 2005). As we show below, our observations suggest the presence of both fast and slow shocks in Serpens SMM1.

5.1.1. Fast Shocks

The bright and velocity-shifted [O I]63 μm emission, together with the detection of [Ne II]12 μm and very high energy [Fe II] lines in Serpens SMM1 suggests the presence of fast dissociative *J*-shocks related with the presence of an embedded atomic jet near the protostar. Note that [Ne II] and [Fe II] lines have been detected towards other YSOs (see *e.g.*, Lahuis et al. 2010, for the c2d *Spitzer* sample). Hollenbach & McKee (1989) presented detailed models for the fine-structure emission of atoms and ions in such dissociative *J*-type shocks. However, the chemistry of S, Fe, Si and related molecules (including gas-phase depletion, *e.g.*, Nisini et al. 2005) were not included and thus the fine-structure absolute line intensity predictions are likely upper limits. In addition, because the beam filling factors of the possible shock components are not known, line ratios provide a much better diagnostic than absolute intensities. According to these detailed models, the observed [Si II]35 μm /[Fe II]26 μm < 1 line intensity ratio (independently on the assumed extinction) provides a lower limit to the pre-shock density, $n_0 = n_0(\text{H}) + 2n_0(\text{H}_2)$, of $> 10^4 \text{ cm}^{-3}$. Besides, owing to the high ionization potential of Ne⁺, the [Ne II]12 μm /[Fe II]26 μm line intensity ratio increases sharply with the shock velocity (v_s). A lower limit of $v_s > 60 \text{ km s}^{-1}$ is found from the observed [Ne II]12 μm /[Fe II]26 μm ≥ 0.1 line ratio (applying an extinction correction of $A_V \geq 30$).

Models of fast dissociative *J*-shocks predict that the gas is initially atomic and very hot (a few thousand K), but by the time that molecules reform, the gas cools to about 400 K. H₂ formation provides the main heat source for this “temperature plateau” (Hollenbach & McKee 1989; Neufeld & Dalgarno 1989). In such models, H₂ is not so abundant and cooling by H₂ and H₂O can be less important than by [O I], CO and OH. Therefore, in addition to the mid-IR fine-structure emission, a significant fraction of the [O I], OH and the CO *warm* component emission can arise behind fast dissociative shocks triggered by a jet impacting the inner, dense envelope.

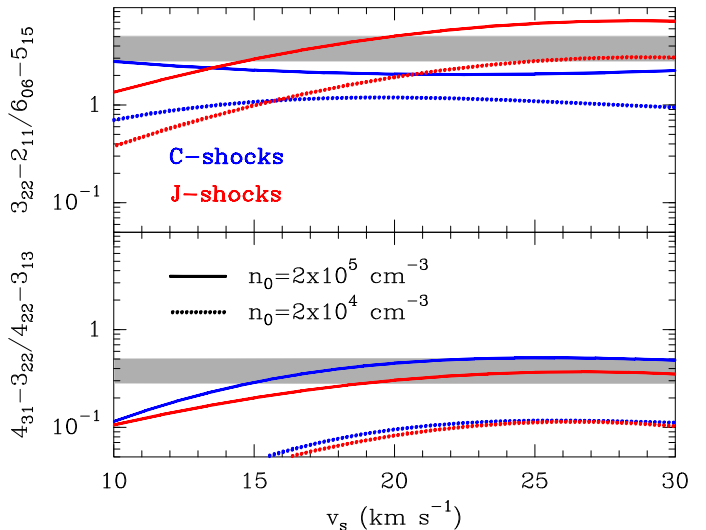


Fig. 10. Comparison of selected *p*-H₂O line intensity ratios observed with PACS and shock model predictions from Flower & Pineau Des Forêts (2010). Red and blue curves represent *J*-type and *C*-type shock models respectively. The pre-shock gas density is $n_0=2\times 10^5 \text{ cm}^{-3}$ (continuous curves) and $n_0=2\times 10^4 \text{ cm}^{-3}$ (dotted curves). Low opacity lines from high energy rotational levels ($E_u/k\sim 300-650 \text{ K}$) observed at similar wavelengths are selected. The *upper* panel shows the *p*-H₂O $3_{22}-2_{11}/6_{06}-5_{15}$ line ratio ($89.988/83.284 \mu\text{m}$) and the *lower* panel shows the $4_{31}-3_{22}/4_{22}-3_{13}$ ($56.325/57.637 \mu\text{m}$) line ratios. The grey horizontal areas show the observed ratios and their error margins.

5.1.2. (UV-irradiated) Slow Shocks

From the observed H₂ 0-0 *S*(2) weak line and the upper limit of the non-detected *S*(0) line, we derive a lower limit to the H₂ rotational temperature (T_{42}) of $\sim 700 \text{ K}$ (if a extinction correction of $A_V=30$ is applied). This (and higher) temperatures of the molecular gas are often inferred behind non-dissociative shocks (*e.g.*, Neufeld et al. 2006; Melnick et al. 2008).

Depending on the shock velocity, non-dissociative *C*-type shocks shielded from UV radiation can produce very high gas temperatures without destroying molecules ($T_k \sim 400-3000 \text{ K}$ for $v_s \sim 10-40 \text{ km s}^{-1}$ in the models by Kaufman & Neufeld 1996). They also naturally produce high H₂O/CO abundance ratios (close to 1) but predict low OH/H₂O $\ll 1$ ratios (owing to negligible H₂O photodissociation but very efficient OH + H₂ \rightarrow H₂O + H reactions in the hot molecular gas). Therefore, a non-dissociative *C*-shock could be the origin of the observed H₂ lines, high-*J* CO ($J_u \gtrsim 30$) and excited H₂O lines ($E_u/k \gtrsim 300 \text{ K}$). Note that in our simple model we infer a high H₂O_{*h*}/CO_{*h*} ≈ 0.4 relative abundance when considering the *hot* component alone. On the other hand, if the *hot* and *warm* components inferred from the ¹²CO rotational diagram only reflect the presence of a temperature gradient in the same physical component, then we would infer much lower H₂O_{*h*}/(CO_{*h*}+CO_{*w*}) ≈ 0.02 abundances (see Table 3). Such low H₂O abundances are difficult to reconcile with non-dissociative *C*-shocks shielded from UV radiation and are more consistent with low-velocity *J*-shocks (see below).

Planar-shock model predictions of absolute H₂O line intensities depend again on the unknown beam filling factor of the shocked material. Figure 10 shows a comparison of selected H₂O line intensity ratios with recent unidimensional models of non-dissociative *C*-type and *J*-type shocks (the latter for $v_s < 30 \text{ km s}^{-1}$) by Flower & Pineau Des Forêts (2010). In order

to avoid using optically thick line diagnostics, different beam dilutions and extinction corrections, we selected low opacity p -H₂O lines arising from high energy levels ($E_u/k \sim 300\text{-}650\text{ K}$) observed at similar wavelengths. The *upper* panel shows the 3₂₂-2₁₁/6₀₆-5₁₅ line ratio (89.988/83.284 μm) and the *lower* panel shows the 4₃₁-3₂₂/4₂₂-3₁₃ (56.325/57.637 μm) line ratio. The grey horizontal areas show the observed line intensity ratios and their error margins. From this comparison we conclude that low-velocity, non-dissociative shocks ($v_s \lesssim 20\text{ km s}^{-1}$) with a pre-shock density of $n_0 \approx 2 \times 10^5\text{ cm}^{-3}$ are needed to reproduce the observed ratios. Figure 10 favors small-scale non-dissociative *J*-shocks, although it is difficult to determine any possible contribution of *C*-type shocks in the frame of current shock models and lack of spectral/angular resolution at $\lambda < 100\text{ }\mu\text{m}$.

Besides, the very different shock velocities required by Ne⁺ versus H₂O lines suggests that both emissions arise from different locations. This will be the case if the Ne⁺ emission arises from fast shocks within the jet itself, but the H₂O (and H₂) emission arises in lower velocity shocks along the inner walls of the outflow cavity. Finally, note that the similar excitation conditions in the hot and dense gas ($P/k = n T_K \approx 8 \times 10^9\text{ K cm}^{-3}$), as well as the similar spatial distribution of the nearby CO $J=29\text{-}28$ and p -H₂O 3₂₂-2₁₁ lines shown in Figure 4 suggests that the *hot* CO and the excited H₂O lines arise in the same shock component.

The UV radiation field probed by the [C II]158 μm line can also heat the gas along the outflow cavity walls (see *e.g.*, Visser et al. 2012). UV photons will modify the chemistry of the shocked gas (*e.g.*, by photodissociating H₂O and enhancing the OH and O abundances; see Sect. 5.3), but in terms of gas heating, they are likely not a dominant heating mechanism of the hot gas emission seen towards low-mass protostars (see Karska et al. submitted). All in all, the relative line intensities of the detected atomic and molecular species confirm the presence of both fast dissociative and lower velocity, non-dissociative shocks that are irradiated by UV radiation fields.

5.2. Line Cooling

Complete far-IR and submm spectral scans allow an unbiased determination of the line cooling in YSOs. Line photons following collisional excitation and escaping the region are responsible of the gas cooling. Hence, the observed line luminosities in a broadband spectral scan provide a good measurement of the total gas cooling budget (see Table 1). In Serpens SMM1, $\sim 54\%$ of the total line luminosity is due to ¹²CO lines, followed by H₂O ($\sim 22\%$ and $L(\text{H}_2\text{O})/L(\text{CO}) \approx 0.4$), [O I] ($\sim 12\%$) and OH (9%). The total far-IR and submm line luminosity $L_{\text{FIR SMM}} = L(\text{CO}) + L(\text{H}_2\text{O}) + L(\text{O}) + L(\text{OH}) + L(\text{CO}) + L(\text{C}^+)$ is $L_{\text{FIR SMM}} \approx 0.12 L_\odot$, and the ratio $L_{\text{mol}}/L_{\text{bol}}$ between the molecular line luminosity, $L_{\text{mol}} = L(\text{CO}) + L(\text{H}_2\text{O}) + L(\text{OH})$, and the bolometric luminosity is $\approx 3.5 \times 10^{-3}$, all consistent with the expected emission of a Class 0 source (see *e.g.*, Giannini et al. 2001). Note that only if the extinction in the mid-IR is larger than $A_V \approx 200$, then the intrinsic luminosity of the observed H₂ lines will be higher than those of CO and H₂O.

In our model, CO dominates the line cooling (Table 1) with more than half of the total CO luminosity arising from the *warm* component (a mixture of shocks and UV-illuminated material) and with a *warm/hot* luminosity ratio of $L(\text{CO}_w)/L(\text{CO}_h) \approx 5$. H₂O is the second most important species, with a dominant contribution to the hot shocked gas cooling. Note that we predict that $\gtrsim 80\%$ of the H₂O line luminosity is radiated in the $55\text{ }\mu\text{m} < \lambda < 200\text{ }\mu\text{m}$ range and only $\sim 5\%$ at shorter wavelengths

(in agreement with the absence of strong H₂O lines in the *Spitzer* observations).

[O I] and OH lines also contribute to the gas cooling. In particular, both the absolute OH luminosities and the observed [O I]63 $\mu\text{m}/\text{H}_2$ 0-0 $S(1) \gg 1$ intensity ratio are too bright for non-dissociative *C*-shock models (Kaufman & Neufeld 1996; Flower & Pineau Des Forêts 2010). As noted before, a significant fraction of the [O I] and OH line emission likely contributes to the cooling behind a fast, dissociative *J*-type shock.

5.3. Shock and UV-driven Chemistry

The plethora of atomic fine-structure lines and to a lesser extent, the relatively high OH/H₂O $\lesssim 0.5$ abundance ratio inferred in the *warm+hot* component, confirms the presence of strong dissociative shocks in the inner envelope. In addition, owing to efficient H₂O photodissociation, an enhanced UV radiation field illuminating the shocked gas can produce a high OH/H₂O abundance ratios (*cf.* Goicoechea et al. 2011, in the Orion Bar PDR). The UV radiation field near low-mass protostars (roughly a diluted $< 10,000\text{ K}$ blackbody) is thought to be dominated by Ly α photons (10.2 eV) arising from accreting material onto the star (Bergin et al. 2003) and from fast dissociative *J*-shocks (Hollenbach & McKee 1979) such as those inferred in Serpens SMM1 (Section 5.1.1). Ly α radiation can dissociate H₂O (producing enhanced OH and O) but can not dissociate CO ($\sim 11.1\text{ eV}$) nor ionize sulfur (10.4 eV) or carbon (11.3 eV) atoms. However, if significant C⁺ and H₂ are present, the ion-neutral drift in *C*-type shocks would significantly enhance the CH⁺ formation rate compared to *J*-type shocks (see Falgarone et al. 2010, for the detection of CH⁺ $J=1\text{-}0$ broad outflow wings in the shock associated with the DR 21 massive star forming region). The lack of CH⁺ $J=3\text{-}2$ emission in Serpens SMM1 provides an upper limit for the CH⁺ column density in the shocked gas (CH^{+)/H₂O < 0.01) and will help to constrain UV-irradiated shocks models (Kaufman et al. in prep.; Lesaffre et al. in prep.). The CH⁺ $J=3\text{-}2$ line is detected in PDRs illuminated by massive OB stars where C⁺ is the dominant carbon species (Goicoechea et al. 2011, Nagy et al. in prep.) and, as in DR 21, the UV radiation field contains photons with energies higher than Ly α (up to 13.6 eV). Excited lines from reactive ions such as CO⁺ (that forms by reaction of C⁺ with OH) and are related with the presence of strong UV radiation fields in the shocked gas, are not detected in the PACS spectrum despite previous tentative assignations of several high-energy far-IR lines (see Ceccarelli et al. 1997, for IRAS 16293-2422)}

The spatial distribution of the [C II]158 μm line emission detected towards Serpens SMM1 (Figure 4) is similar to that of other species in the outflow (with brighter emission in the outflow position than towards the protostar itself). The detection of faint C⁺ emission indicates the presence of a relatively weak UV field (but able to ionize C atoms and dissociate CO) along the outflow. Besides, the increase of the HCO⁺/HCN abundance ratio in the *warm* temperature component (HCN is easily photodissociated while HCO⁺ is abundant in the dense gas directly exposed to strong UV radiation) is another signature of UV photons. Indeed, the mere detection of [C I]370, 609 μm lines at the poor spectral resolution of the SPIRE-FTS towards the protostar shows that [C I] lines are significantly brighter than towards HH46 (van Kempen et al. 2009) or NGC1333 IRAS 4A/4B (Yıldız et al. 2012). The presence of weak C⁺ line emission and of Ly α radiation in protostars like Serpens SMM1 (although difficult to detect) suggests that *UV-irradiated shocks are a common phenomenon in YSOs*.

X-ray emission is also expected in low-mass YSOs (Stäuber et al. 2006, 2007; Feigelson 2010) and they produce *internally* generated UV radiation fields after collisions of energetic photoelectrons with H and H₂ (Maloney et al. 1996; Hollenbach & Gorti 2009). Although X-ray detections with *Chandra* have been reported towards the nearby Serpens SMM5, SMM6 and S68Nb protostars (Winston et al. 2007), the strength of any X-ray emission from Serpens SMM1 is unknown, possibly because of the high column density to the embedded source.

High sensitivity and velocity-resolved observations of CH⁺, CO⁺, SO⁺ and other reactive ions related with the presence of ionized atoms (*e.g.*, C⁺ and S⁺) will help us to characterize these UV-irradiated shocks in more detail.

5.4. Comparison with Other Low-Mass Protostars

Comparative spectroscopy of protostars in different stages of evolution allows us to identify the common and the more peculiar processes associated with the first stages of star formation. Comparing the far-IR spectrum of the NGC 1333 IRAS 4B outflow to that of the Serpens SMM1 protostar, both show similar high H₂O luminosities ($L(\text{H}_2\text{O}) \sim 0.03 L_{\odot}$). However, Serpens SMM1 shows a factor ~ 50 stronger [O I] luminosity and a lower $L(\text{H}_2\text{O})/L(\text{CO})$ ratio. The weak [O I] emission and high H₂O luminosity in IRAS 4B outflow ($L(\text{H}_2\text{O})/L(\text{CO}) \approx 1$) has been interpreted as non-dissociative C-shocks shielded from UV radiation (Herczeg et al. 2012). Indeed, C⁺ is not detected in IRAS 4B outflow whereas it is detected in Serpens SMM1 protostar and outflow (see Figure 4). On the other hand, the strong [O I] and OH emission towards the Serpens SMM1 protostar itself is more similar to that of Class I source HH46 (van Kempen et al. 2010) where a $L(\text{OH})/L(\text{H}_2\text{O}) \approx 0.5$ luminosity ratio has been inferred (*vs.* ~ 0.4 in SMM1). One possibility is that a high-velocity jet impinging on the dense inner envelope produces dissociative J-shocks (van Kempen et al. 2010) and enhanced [O I] and OH emission compared to non-dissociative C-shocks. Although they could not distinguish the dominant scenario, either J-shocks or UV-irradiated C-shocks have been also proposed to explain the OH emission seen in the high-mass YSO W3 IRS 5 (Wampfler et al. 2011).

The detection of [Ne II], [Fe II], [Si II] and [S I] fine-structure lines towards Serpens SMM1 reinforces the scenario of both fast and slow shocks as well as UV radiation near the protostar, however, it is difficult to extract the exact geometry of the different shock components in the circumstellar environment (*e.g.*, Ne⁺ versus H₂O line emitting regions). Note that the presence of an embedded jet in the Class 0 source L1448 was reported from the detection of [Fe II] and [Si II] lines by Dionatos et al. (2009), and the same lines have been detected towards the nearby YSOs Serpens SMM3 and SMM4 (Lahuis et al. 2010). However, they did not detect the [Ne II]12.8 μm line that requires fast shock velocities (Lahuis et al. 2007; Baldovin-Saavedra et al. 2012) or X-ray radiation (see Güdel et al. 2010, for Class II disk sources).

Compared to HH46, CO lines with $J_u > 30$ and higher excitation H₂O lines are detected in Serpens SMM1 (not necessarily due to different excitation conditions but maybe just because lines are much brighter in SMM1). We have proposed that this *hot* CO and H₂O emission arises from low velocity, non-dissociative shocks in the inner walls of the outflow cavity compressing the gas to very high thermal pressures ($P/k = n T_K \approx 10^{9-10} \text{ K cm}^{-3}$). Based on the large gas compression factors and H₂O line profiles seen toward several shock spots in bipolar outflows (far from the protostellar sources) Santangelo et al. (2012) and Tafalla et al. (in prep.) also conclude that cur-

rent low velocity J-shocks models explain their observations better than stationary C-shocks models. New shock models with a more detailed geometrical description and including the effects of UV radiation are clearly needed to determine the exact nature of the shocks inferred in the dense circumstellar gas near protostars.

The *warm* CO line emission ($15 \lesssim J_u \lesssim 25$) observed in Serpens SMM1 is a common feature in the far-IR spectrum of most protostars even if they are in different stages of evolution. This was previously observed by ISO (*e.g.*, Giannini et al. 2001) and now by *Herschel* (*e.g.*, Karska et al. submitted.; Green et al. in prep., Manoj et al., in prep.). This CO emission *ubiquity* necessarily means that a broad combination of shock velocities and densities can produce a similar *warm* CO spectrum in different low- and high-mass YSOs.

The $L(\text{OH})/L(\text{H}_2\text{O})$, $L(\text{CO})/L(\text{[O I]})$ and $L(\text{H}_2\text{O})/L(\text{[O I]})$ luminosity ratios in Serpens SMM1 have intermediate values between those in NGC 1333 IRAS 4B Class 0 YSO and HH46 Class I YSO (with ratios closer to SMM1) suggesting that the different luminosity ratios in IRAS 4B outflow are either a consequence of an earlier stage of evolution, or simply because the IRAS 4B outflow is peculiar, with very high H₂O abundances not affected by UV photodissociation. Indeed, one of the main conclusions of all these studies is that *water vapour lines are a robust probe of shocked gas in protostellar environments*. In Serpens SMM1 we infer a total $\text{H}_2\text{O}_h/(\text{CO}_h + \text{CO}_w) \approx 0.02$ abundance ratio in the *warm+hot* components traced by our far-IR observations. Only if the *hot* component was an independent physical component, the H₂O abundances would be much higher ($\text{H}_2\text{O}_h/\text{CO}_h \approx 0.4$). However, this value is higher than the typical H₂O/CO abundance ratios inferred from HIFI observations of the ground-state *o*-H₂O 1₁₀-1₀₁ line (at ~ 557 GHz) towards a large sample of low-mass protostars (Kristensen et al. 2012). In these velocity-resolved observations, the H₂O/CO abundance ratio increases from $\sim 10^{-3}$ at low outflow velocities ($< 5 \text{ km s}^{-1}$) to ~ 0.1 at high outflow velocities ($> 10 \text{ km s}^{-1}$). Therefore, our inferred abundance ratio of $\text{H}_2\text{O}_h/(\text{CO}_h + \text{CO}_w) \approx 0.02$ from PACS observations seems a better description of the water vapour abundance in the protostellar shocked gas. Besides, it is also consistent with recent determinations from velocity-resolved HIFI observations of moderately excited H₂O lines ($E_u/k < 215 \text{ K}$) (see *e.g.*, Santangelo et al. 2012, for L1448 outflow).

6. Summary and Conclusions

We have presented the first complete far-IR and submm spectrum of a Class 0 protostar (Serpens SMM1) taken with *Herschel* in the ~ 55 - $671 \mu\text{m}$ window. The data are complemented with mid-IR spectra in the ~ 10 - $37 \mu\text{m}$ window retrieved from the *Spitzer* archive and first discussed here. These spectroscopic observations span almost 2 decades in wavelength and allow us to unveil the most important heating and chemical processes associated with the first evolutionary stages of low-mass protostars. In particular, we obtained the following results:

- Serpens SMM1 shows a very rich far-IR and submm emission spectrum, with more than 145 lines, most of them rotationally excited lines of ¹²CO (up to $J=42$ - 41), H₂O, OH, ¹³CO, HCN, HCO⁺ and weaker emission from [C II]158 and [C I]370, 609 μm. [O I]63 μm is the brightest line. Approximately half of the total far-IR and submm line luminosity is provided by CO rotational emission, with important contribution from H₂O (~22%), [O I] (~12%) and OH (~9%).

- The mid-IR spectrum shows many fewer lines (probably due to severe dust extinction and lack of spectral resolution). Bright fine structure lines from Ne^+ , Fe^+ , Si^+ , and S, as well as weak H_2S (1) and S(2) pure rotational lines are detected.

- The ^{12}CO rotational diagram suggests the presence of 3 temperature components with $T_{\text{rot}}^{\text{hot}} \approx 620 \pm 30 \text{ K}$, $T_{\text{rot}}^{\text{warm}} \approx 340 \pm 40 \text{ K}$ and $T_{\text{rot}}^{\text{cool}} \approx 100 \pm 15 \text{ K}$. As predicted by SED models in the literature, the detection of H_2O , OH, HCO^+ and HCN emission lines from very high critical density transitions suggests that the density in the inner envelope is high ($n(\text{H}_2) \gtrsim 5 \times 10^6 \text{ cm}^{-3}$), and thus the CO rotational temperatures provide a good approximation to the gas temperature ($T_{\text{rot}} \lesssim T_k$).

- A non-LTE, multi-component model allowed us to approximately quantify the contribution of the different temperature components ($T_k^{\text{hot}} \approx 800 \text{ K}$, $T_k^{\text{warm}} \approx 375 \text{ K}$ and $T_k^{\text{cool}} \approx 150 \text{ K}$) and to estimate relative chemical abundances. The detected mid-IR H_2 lines provide a lower limit to H_2 column density of $N_{\text{H}_2} \geq 10^{22} \text{ cm}^{-2}$. We derive the following upper limit abundances with respect to H_2 in the *hot+warm* components: $x(\text{CO}) \leq 10^{-4}$, $x(\text{H}_2\text{O}) \leq 0.5 \times 10^{-5}$ and $x(\text{OH}) \leq 10^{-6}$. The inferred water vapour abundance is higher than the value typically found in cold interstellar clouds but lower than that expected in hot shocked gas completely shielded from UV radiation

- Excited CO, H_2O and OH emission lines arising from high energy levels are detected (up to $E_u/k = 4971 \text{ K}$, $E_u/k = 1036 \text{ K}$ and $E_u/k = 618 \text{ K}$ respectively). These species arise in the *hot+warm* gas ($M \lesssim 0.03 M_\odot$) that we associate with a mixture of shocks. The observed *hot* CO, H_2O and H_2 lines provide a lower limit to the gas temperature of $\sim 700 \text{ K}$. The excited H_2O line emission is consistent with detailed model predictions of low-velocity non-dissociative shocks (with $v_s \lesssim 20 \text{ km s}^{-1}$).

- Fast dissociative (and ionizing) shocks with velocities $v_s > 60 \text{ km s}^{-1}$ and pre-shock densities $\geq 10^4 \text{ cm}^{-3}$ related with the presence of an embedded atomic jet are needed to explain the observed Ne^+ , Fe^+ , Si^+ and S fine-structure emission and also the bright and velocity-shifted [O I]63 μm line emission. Dissociative *J*-shocks produced by the jet impacting the ambient material are the most probable origin of the bright [O I] and OH emission and of a significant fraction of the *warm* CO emission. In addition, water vapour photodissociation in UV-irradiated non-dissociative shocks along the outflow cavity walls can also contribute to the [O I] and OH emission.

Compared to other protostars, the large number of lines detected towards Serpens SMM1 reveals the great complexity of the protostellar environment. Both fast and slow shocks are needed to explain the presence of atomic fine structure lines and high excitation molecular lines. The spectra also show the signature of UV radiation (C⁺ and C towards the protostar and outflow). Therefore, most species (including H_2O , OH, O and trace molecules such as CH⁺) arise in shocked gas illuminated by UV (even X-ray) radiation fields. Irradiated shocks are likely a very common phenomenon in YSOs.

Acknowledgements. We acknowledge our WISH internal referees, D. Neufeld and P. Bjerkeli for very helpful comments on an earlier version of the manuscript. We also thank the entire WISH team for many useful and vivid discussions in the last years. We finally thank the anonymous referee and M. Walmsley for useful comments. WISH research in Leiden is supported by the Netherlands Research School for Astronomy (NOVA), by a Spinoza grant and grant 614.001.008 from the Netherlands Organisation for Scientific Research (NWO), and by EU-FP7 grant 238258 (LASSIE). JRC, JC and ME thank the Spanish MINECO for funding support through grants AYA2009-07304 and CSD2009-00038. JRG is supported by a Ramón y Cajal research contract from the MINECO and co-financed by the European Social Fund.

References

- Bachiller, R. & Tafalla, M. 1999, in NATO ASIC Proc. 540: The Origin of Stars and Planetary Systems, ed. C. J. Lada & N. D. Kylafis, 227
- Baldovin-Saavedra, C., Audard, M., Carmona, A., et al. 2012, A&A, 543, A30
- Bergin, E., Calvet, N., D'Alessio, P., & Herczeg, G. J. 2003, ApJ, 591, L159
- Bontemps, S., Andre, P., Terebey, S., & Cabrit, S. 1996, A&A, 311, 858
- Caselli, P., Keto, E., Pagani, L., et al. 2010, A&A, 521, L29
- Ceccarelli, C., Caux, E., Wolfire, M., et al. 1997, in ESA Special Publication, Vol. 419, The first ISO workshop on Analytical Spectroscopy, ed. A. M. Heras, K. Leech, N. R. Trams, & M. Perry, 43
- Cernicharo, J. 2012, in European Astronomical Society Publications Series, Vol. 2012, Proceedings of the European Conference on Laboratory Astrophysics, ed. C. Stehlé, C. Joblin, & L. d'Hendecourt, 4
- Cernicharo, J., Goicoechea, J. R., Daniel, F., et al. 2006, ApJ, 649, L33
- Chiar, J. E., Ennico, K., Pendleton, Y. J., et al. 2007, ApJ, 666, L73
- Davis, C. J., Matthews, H. E., Ray, T. P., Dent, W. R. F., & Richer, J. S. 1999, MNRAS, 309, 141
- Dionatos, O., Nisini, B., Codella, C., & Giannini, T. 2010, A&A, 523, A29
- Dionatos, O., Nisini, B., Garcia Lopez, R., et al. 2009, ApJ, 692, 1
- Draine, B. T. & McKee, C. F. 1993, ARA&A, 31, 373
- Dzib, S., Loinard, L., Mioduszewski, A. J., et al. 2010, ApJ, 718, 610
- Eiroa, C., Djupvik, A. A., & Casali, M. M. 2008, The Serpens Molecular Cloud, ed. B. Reipurth, 693
- Enoch, M. L., Corder, S., Dunham, M. M., & Duchêne, G. 2009, ApJ, 707, 103
- Evans, II, N. J., Dunham, M. M., Jørgensen, J. K., et al. 2009, ApJS, 181, 321
- Falgarone, E., Ossenkopf, V., Gerin, M., et al. 2010, A&A, 518, L118
- Feigelson, E. D. 2010, Proceedings of the National Academy of Science, 107, 7153
- Flower, D. R. & Pineau Des Forets, G. 2010, MNRAS, 406, 1745
- Giannini, T., Nisini, B., & Lorenzetti, D. 2001, ApJ, 555, 40
- Goicoechea, J. R. & Cernicharo, J. 2002, ApJ, 576, L77
- Goicoechea, J. R., Cernicharo, J., Lerote, M. R., et al. 2006, ApJ, 641, L49
- Goicoechea, J. R., Joblin, C., Contursi, A., et al. 2011, A&A, 530, L16
- Griffin, M. J., Abergerl, A., Abreu, A., et al. 2010, A&A, 518, L3
- Güdel, M., Lahuis, F., Briggs, K. R., et al. 2010, A&A, 519, A113
- Herczeg, G. J., Karska, A., Bruderer, S., et al. 2012, A&A, 540, A84
- Hogerheijde, M. R., van Dishoeck, E. F., Salverda, J. M., & Blake, G. A. 1999, ApJ, 513, 350
- Hollenbach, D. & Gorti, U. 2009, ApJ, 703, 1203
- Hollenbach, D. & McKee, C. F. 1979, ApJS, 41, 555
- Hollenbach, D. & McKee, C. F. 1989, ApJ, 342, 306
- Houck, J. R., Roellig, T. L., van Cleve, J., et al. 2004, ApJS, 154, 18
- Kaufman, M. J. & Neufeld, D. A. 1996, ApJ, 456, 611
- Kristensen, L. E., van Dishoeck, E. F., Bergin, E. A., et al. 2012, A&A, 542, A8
- Lahuis, F., van Dishoeck, E. F., Blake, G. A., et al. 2007, ApJ, 665, 492
- Lahuis, F., van Dishoeck, E. F., Jørgensen, J. K., Blake, G. A., & Evans, N. J. 2010, A&A, 519, A3
- Langer, W. D. & Penzias, A. A. 1990, ApJ, 357, 477
- Laor, A. & Draine, B. T. 1993, ApJ, 402, 441
- Larsson, B., Liseau, R., & Men'shchikov, A. B. 2002, A&A, 386, 1055
- Larsson, B., Liseau, R., Men'shchikov, A. B., et al. 2000, A&A, 363, 253
- Maloney, P. R., Hollenbach, D. J., & Tielens, A. G. G. M. 1996, ApJ, 466, 561
- Melnick, G. J., Tolls, V., Neufeld, D. A., et al. 2008, ApJ, 683, 876
- Neufeld, D. A. & Dalgarno, A. 1989, ApJ, 340, 869
- Neufeld, D. A., Melnick, G. J., Sonnentrucker, P., et al. 2006, ApJ, 649, 816
- Nisini, B., Bacciotti, F., Giannini, T., et al. 2005, A&A, 441, 159
- Offer, A. R. & van Dishoeck, E. F. 1992, MNRAS, 257, 377
- Pilbratt, G. L., Riedinger, J. R., Passvogel, T., et al. 2010, A&A, 518, L1
- Poglitsch, A., Waelkens, C., Geis, N., et al. 2010, A&A, 518, L2
- Rodríguez, L. F., Loinard, L., D'Alessio, P., Wilner, D. J., & Ho, P. T. P. 2005, ApJ, 621, L133
- Santangelo, G., Nisini, B., Giannini, T., et al. 2012, A&A, 538, A45
- Smith, J. D. T., Armus, L., Dale, D. A., et al. 2007, PASP, 119, 1133
- Stäuber, P., Benz, A. O., Jørgensen, J. K., et al. 2007, A&A, 466, 977
- Stäuber, P., Jørgensen, J. K., van Dishoeck, E. F., Doty, S. D., & Benz, A. O. 2006, A&A, 453, 555
- van Dishoeck, E. F., Kristensen, L. E., Benz, A. O., et al. 2011, PASP, 123, 138
- van Kempen, T. A., Kristensen, L. E., Herczeg, G. J., et al. 2010, A&A, 518, L121
- van Kempen, T. A., van Dishoeck, E. F., Hogerheijde, M. R., & Güsten, R. 2009, A&A, 508, 259
- Visser, R., Kristensen, L. E., Bruderer, S., et al. 2012, A&A, 537, A55
- Walmsley, M., Pineau des Forêts, G., & Flower, D. 2005, in IAU Symposium, Vol. 231, Astrochemistry: Recent Successes and Current Challenges, ed. D. C. Lis, G. A. Blake, & E. Herbst, 135–140
- Wampfler, S. F., Bruderer, S., Kristensen, L. E., et al. 2011, A&A, 531, L16
- Watson, D. M., Bohac, C. J., Hull, C., et al. 2007, Nature, 448, 1026

Whittet, D. C. B., ed. 2003, Dust in the galactic environment
Winston, E., Megeath, S. T., Wolk, S. J., et al. 2007, ApJ, 669, 493
Yıldız, U. A., Kristensen, L. E., van Dishoeck, E. F., et al. 2012, A&A, 542, A86

Appendix A: Complementary Figures and Tables

Table A.1. List of detected lines towards Serpens SMM1 and line fluxes from SPIRE and PACS central spaxels (corrected for extended emission in the case of PACS). The horizontal line near $\sim 300\text{ }\mu\text{m}$ shows the transition between the SPIRE SLW and SSW detector arrays (beams between $42''$ and $17''$). The line near $\sim 200\text{ }\mu\text{m}$ marks the lines detected with PACS (spaxel size $\sim 9.4''$). Lines in the PACS ranges with detector leakage are not tabulated. Flux errors up to $\sim 30\%$. Both the o -H₂O 1_{01} and p -H₂O 0_{00} ground-state levels are at $E_{\text{low}}/k=0$.

Species	Transition	E_{up} (K)	λ (μm)	Line Flux (W m^{-2})
HCO ⁺	5 - 4	64.2	672.326	2.24E-16
CO	4 - 3	55.3	650.252	4.11E-16
C	3P_1 - 3P_0	23.6	609.133	8.69E-17
HCO ⁺	6 - 5	89.9	560.294	3.16E-17
¹³ CO	5 - 4	79.3	544.161	6.33E-17
H ₂ O	1_{10} - 1_{01}	26.7	538.289	4.96E-17
CO	5 - 4	83.0	520.231	5.13E-16
HCO ⁺	7 - 6	119.8	480.275	6.20E-17
¹³ CO	6 - 5	111.1	453.498	1.11E-16
CO	6 - 5	116.2	433.556	6.85E-16
HCN	8 - 7	153.1	422.912	3.28E-17
HCO ⁺	8 - 7	154.1	420.263	5.51E-17
H ₂ O	2_{11} - 2_{02}	136.9	398.643	1.67E-16
¹³ CO	7 - 6	148.1	388.743	1.42E-16
HCO ⁺	9 - 8	192.6	373.591	4.10E-17
CO	7 - 6	154.9	371.650	1.32E-15
C	3P_2 - 3P_1	62.5	370.414	1.42E-16
¹³ CO	8 - 7	190.4	340.181	4.16E-17
HCO ⁺	10 - 9	235.4	336.255	3.37E-17
CO	8 - 7	199.1	325.225	1.68E-15
HCN	11 - 10	280.7	307.641	5.55E-17
HCO ⁺	11 - 10	282.4	305.712	8.91E-17
H ₂ O	2_{02} - 1_{11}	100.8	303.459	4.40E-16
¹³ CO	9 - 8	237.9	302.415	1.59E-16
CO	9 - 8	248.9	289.120	1.54E-15
HCO ⁺	12 - 11	333.8	280.257	8.18E-17
H ₂ O	3_{12} - 3_{03}	215.2	273.193	3.23E-16
¹³ CO	10 - 9	290.8	272.205	5.62E-17
H ₂ O	1_{11} - 0_{00}	53.4	269.273	4.41E-16
CO	10 - 9	304.2	260.240	2.02E-15
H ₂ O	3_{21} - 3_{12}	271.0	257.790	2.48E-16
¹³ CO	11 - 10	348.9	247.490	1.51E-16
H ₂ O	2_{20} - 2_{11}	195.9	243.972	2.92E-17
CO	11 - 10	365.0	236.613	2.17E-15
¹³ CO	12 - 11	412.4	226.898	7.67E-17
CO	12 - 11	431.3	216.927	2.45E-15
¹³ CO	13 - 12	481.0	209.476	1.51E-16
CO	13 - 12	503.6	200.272	2.60E-15
¹³ CO	14 - 13	555.0	194.546	1.32E-16
H ₂ O	4_{13} - 4_{04}	396.4	187.110	5.74E-17
CO	14 - 13	581.0	185.999	1.55E-15
¹³ CO	15 - 14	634.2	181.608	6.57E-17
H ₂ O	2_{21} - 2_{12}	159.9	180.488	5.25E-16
H ₂ O	2_{12} - 1_{01}	80.1	179.527	9.72E-16
H ₂ O	3_{03} - 2_{12}	162.5	174.626	1.21E-15
CO	15 - 14	663.9	173.631	2.20E-15
¹³ CO	16 - 15	718.7	170.290	3.63E-17
OH	$^2\Pi_{1/2}$ $J=3/2^-$ - $1/2^+$	269.8	163.396	1.92E-16
OH	$^2\Pi_{1/2}$ $J=3/2^+$ - $1/2^-$	270.2	163.015	2.76E-16
CO	16 - 15	752.4	162.812	2.01E-15
U		161.808 ^a	3.49E-17	
C ⁺	$^2P_{3/2}$ - $^2P_{1/2}$	91.2	157.741	2.92E-16
H ₂ O	3_{22} - 3_{13}	296.8	156.194	3.16E-16
CO	17 - 16	846.3	153.267	2.15E-15
O	3P_0 - 3P_1	326.6	145.525	8.38E-16
CO	18 - 17	945.8	144.784	2.04E-15
H ₂ O	3_{13} - 2_{02}	204.7	138.527	9.49E-16

^(a) Observed wavelength (otherwise rest wavelengths are tabulated)

Table A.2. Continuation of Table 1.

Species	Transition	E_{up} (K)	λ (μm)	Line Flux (W m^{-2})
CO	19 - 18	1050.7	137.196	1.66E-15
H ₂ O	5_{14} - 5_{05}	540.5	134.935	1.67E-16
U			132.982 ^a	1.13E-16
U			132.672 ^a	1.76E-16
H ₂ O	4_{23} - 4_{14}	397.9	132.407	3.95E-16
CO	20 - 19	1161.2	130.369	1.62E-15
H ₂ O	4_{04} - 3_{13}	319.5	125.353	6.79E-16
CO	21 - 20	1277.1	124.193	2.01E-15
OH	$^2\Pi_{3/2}$ $J=5/2^+$ - $3/2^-$	120.5	119.441	8.18E-16
OH	$^2\Pi_{3/2}$ $J=5/2^-$ - $3/2^+$	120.8	119.234	8.75E-16
CO	22 - 21	1398.6	118.581	1.29E-15
H ₂ O	4_{14} - 3_{03}	289.3	113.537	7.39E-17 [†]
CO	23 - 22	1525.5	113.458	blended [†]
CO	24 - 23	1657.9	108.763	1.08E-15
H ₂ O	2_{21} - 1_{10}	159.9	108.073	1.35E-16
CO	27 - 26	2087.9	96.773	9.06E-16
U			96.633 ^a	6.14E-17
OH	$^2\Pi_{1/2}$ - $^2\Pi_{3/2}$ $J=3/2^-$ - $5/2^+$	269.8	96.363	2.35E-16
OH	$^2\Pi_{1/2}$ - $^2\Pi_{3/2}$ $J=3/2^+$ - $5/2^-$	270.2	96.271	2.35E-16
H ₂ O	5_{15} - 4_{04}	470.0	95.626	5.16E-16
H ₂ O	4_{41} - 4_{32}	668.1	94.703	1.76E-16
CO	28 - 27	2242.2	93.349	7.55E-16
U			90.574 ^a	4.19E-17
U			90.434 ^a	4.64E-18
CO	29 - 28	2401.9	90.163	6.57E-16
H ₂ O	3_{22} - 2_{11}	296.8	89.988	8.29E-16
CO	30 - 29	2567.0	87.190	7.03E-16
H ₂ O	7_{16} - 7_{07}	979.0	84.766	1.06E-16
OH	$^2\Pi_{3/2}$ $J=7/2^-$ - $5/2^+$	290.5	84.597	9.29E-16
CO	31 - 30	2737.6	84.411	1.25E-15 [†]
OH	$^2\Pi_{3/2}$ $J=7/2^+$ - $5/2^-$	291.2	84.420	blended [†]
H ₂ O	6_{06} - 5_{15}	642.7	83.283	1.69E-16
H ₂ O	6_{16} - 5_{05}	609.3	82.031	5.55E-16
CO	32 - 31	2913.7	81.806	3.84E-16
U			81.013 ^a	7.03E-17
CO	33 - 32	3095.1	79.360	2.49E-16
OH	$^2\Pi_{1/2}$ - $^2\Pi_{3/2}$ $J=1/2^+$ - $3/2^-$	181.7	79.179	blended [†]
OH	$^2\Pi_{1/2}$ - $^2\Pi_{3/2}$ $J=1/2^-$ - $3/2^+$	181.9	79.116	9.97E-16 [†]
H ₂ O	4_{23} - 3_{12}	397.9	78.741	4.89E-17
CO	34 - 33	3282.0	77.059	3.97E-16
H ₂ O	3_{21} - 2_{12}	271.0	75.380	7.23E-16
CO	35 - 34	3474.3	74.890	3.53E-16
U			69.840 ^a	5.75E-17
CO	38 - 37	4083.5	69.074	1.57E-16
CO	39 - 38	4297.3	67.336	1.28E-16
H ₂ O	3_{03} - 3_{03}	376.4	67.269	7.77E-17
H ₂ O	3_{31} - 2_{20}	410.4	67.089	1.90E-16
H ₂ O	3_{30} - 2_{21}	376.4	66.437	4.74E-16
H ₂ O	7_{16} - 6_{25}	979.0	66.092	1.28E-16
CO	40 - 39	4516.6	65.686	8.33E-17
OH	$^2\Pi_{3/2}$ $J=9/2^+$ - $7/2^-$	511.0	65.279	4.45E-16
H ₂ O	6_{25} - 5_{14}	761.3	65.165	1.99E-16
OH	$^2\Pi_{3/2}$ $J=9/2^-$ - $7/2^+$	512.1	65.132	4.11E-16
CO	41 - 40	4741.2	64.117	1.23E-16
H ₂ O	8_{08} - 7_{17}	1070.6	63.457	2.81E-17
H ₂ O	8_{18} - 7_{07}	1036.5	63.322	4.00E-17
O	3P_1 - 3P_2	227.7	63.183	8.34E-15
CO	42 - 41	4971.1	62.624	6.82E-17
U			62.003 ^a	9.05E-17
H ₂ O	7_{26} - 6_{15}	1021.8	59.986	1.40E-16
H ₂ O	4_{32} - 3_{21}	516.1	58.698	2.59E-16
H ₂ O	4_{22} - 3_{13}	454.4	57.636	2.64E-16
H ₂ O	4_{31} - 3_{22}	552.3	56.324	1.05E-16
U			55.481 ^a	8.01E-17

^(a) Observed wavelength (otherwise rest wavelengths are tabulated)

Table A.3. Mid-IR lines detected with *Spitzer*/IRS towards the Class 0 protostar Serpens SMM1 and line fluxes (uncorrected for extinction) within a $7'' \times 7''$ aperture. The horizontal line shows the transition between the LH and SH modules. Intensity errors up to $\sim 25\%$.

Species	Transition	E_{up} (K)	λ (μm)	Line Flux (W m^{-2})
Fe ⁺	$^6D_{5/2}-^6D_{7/2}$	961	35.349	2.45E-17
Si ⁺	$^2P_{3/2}-^2P_{1/2}$	414	34.815	6.29E-17
<i>p</i> -H ₂	0-0 <i>S</i> (0) $J=2-0$	509	28.219	<5.92E-18
Fe ⁺	$^6D_{7/2}-^6D_{9/2}$	554	25.988	8.12E-17
S	$^3P_1-^3P_2$	570	25.249	3.24E-17
Fe ⁺	$^4F_{5/2}-^4F_{7/2}$	4087	24.519	4.46E-17
Fe ⁺	$^4F_{7/2}-^4F_{9/2}$	3499	17.936	1.36E-17
<i>o</i> -H ₂	0-0 <i>S</i> (1) $J=3-1$	1015	17.035	5.96E-19
Ne ⁺	$^2P_{1/2}-^2P_{3/2}$	1124	12.814	7.06E-18
<i>p</i> -H ₂	0-0 <i>S</i> (2) $J=4-2$	1682	12.279	2.42E-18

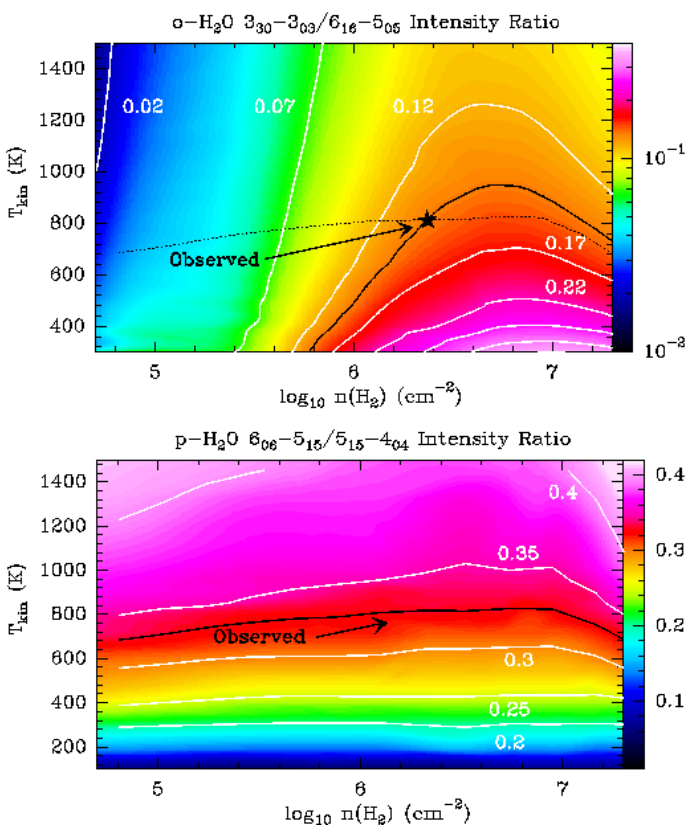


Fig. A.1. Grid of H₂O LVG models for different gas temperatures and densities. *Bottom:* Contour levels of the *p*-H₂O $6_{06}-5_{15}/5_{15}-4_{04}$ ($83.284/95.627\mu\text{m}$) line ratio for $N(p\text{-H}_2\text{O})=10^{16}\text{ cm}^{-2}$. Note the gas temperature dependence of this ratio. The black continuous curve shows the observed intensity line ratio of 0.33. *Top:* Contour levels of the *o*-H₂O $3_{30}-3_{03}/6_{16}-3_{05}$ ($67.269/82.031\mu\text{m}$) ratio for $N(o\text{-H}_2\text{O})=3\times 10^{16}\text{ cm}^{-2}$. Note the gas density dependence of this ratio. The black continuous curve shows the observed intensity line ratio of 0.14 while the black dotted curve shows the observed *p*-H₂O $6_{06}-5_{15}/5_{15}-4_{04}$ ratio. The intersection of both curves is marked with a star.

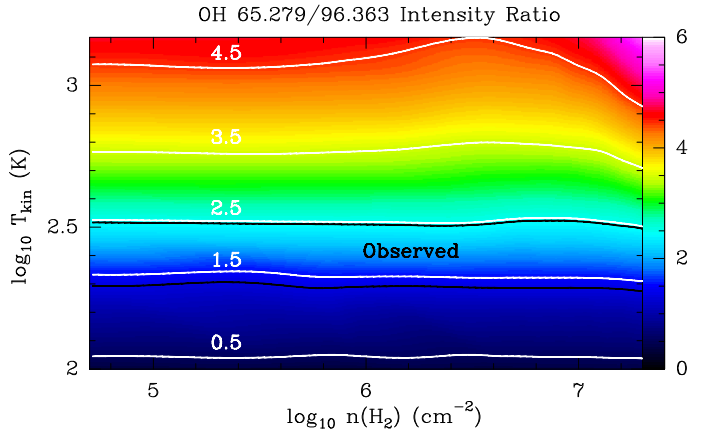


Fig. A.2. Grid of OH LVG models for different gas temperatures and densities. Contour levels of the OH $^2\Pi_{3/2} J=9/2^+-7/2^-/^2\Pi_{1/2} J=3/2^-/5/2^+$ ($65.279/96.363\mu\text{m}$) line ratio for $N(\text{OH})=10^{16}\text{ cm}^{-2}$. Note the gas temperature dependence of this ratio. The black continuous curves enclose the observed intensity line ratio with a $\sim 15\%$ of relative flux calibration error.

-
- ¹ Centro de Astrobiología (CSIC/INTA), Ctra. de Torrejón a Ajalvir,
km 4 28850, Torrejón de Ardoz, Madrid, Spain.
e-mail: jr.goicoechea@cab.inta-csic.es
- ² Max-Planck-Institut für extraterrestrische Physik (MPE), Postfach
1312, 85741 Garching, Germany.
- ³ Leiden Observatory, Leiden University, PO Box 9513, 2300 RA
Leiden, The Netherlands.
- ⁴ Kavli Institute for Astronomy and Astrophysics, Peking University,
Yi He Yuan Lu 5, HaiDian Qu, 100871 Beijing, China.
- ⁵ RAL Space, Rutherford Appleton Laboratory, Chilton, Didcot,
Oxfordshire, OX11 0QX, UK.
- ⁶ Institute for Space Imaging Science, University of Lethbridge, 4401
University Drive, Lethbridge, Alberta, T1J 1B1, Canada.
- ⁷ Centre for Star and Planet Formation, Natural History Museum of
Denmark, University of Copenhagen, Øster Voldgade 5-7, DK-1350
København K, Denmark.
- ⁸ Université de Toulouse; UPS-OMP; IRAP; Toulouse, France.
- ⁹ CNRS; IRAP; 9 Av. colonel Roche, BP 44346, F-31028 Toulouse
cedex 4, France
- ¹⁰ Department of Astronomy, University of Michigan, 500 Church St.,
Ann Arbor, MI 48109, USA

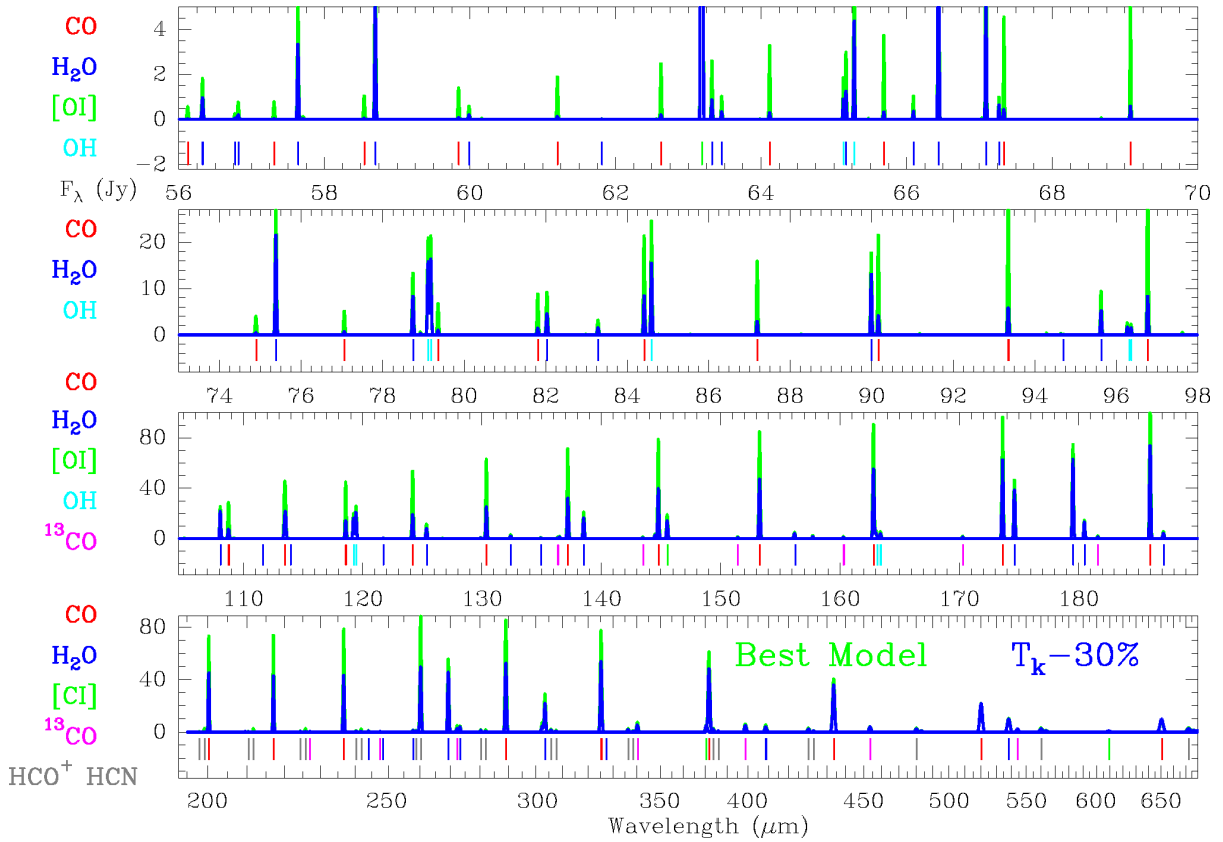


Fig. A.3. Best model discussed in the text (green curves) and a model where T_k is decreased by 30% in all components (blue curves).

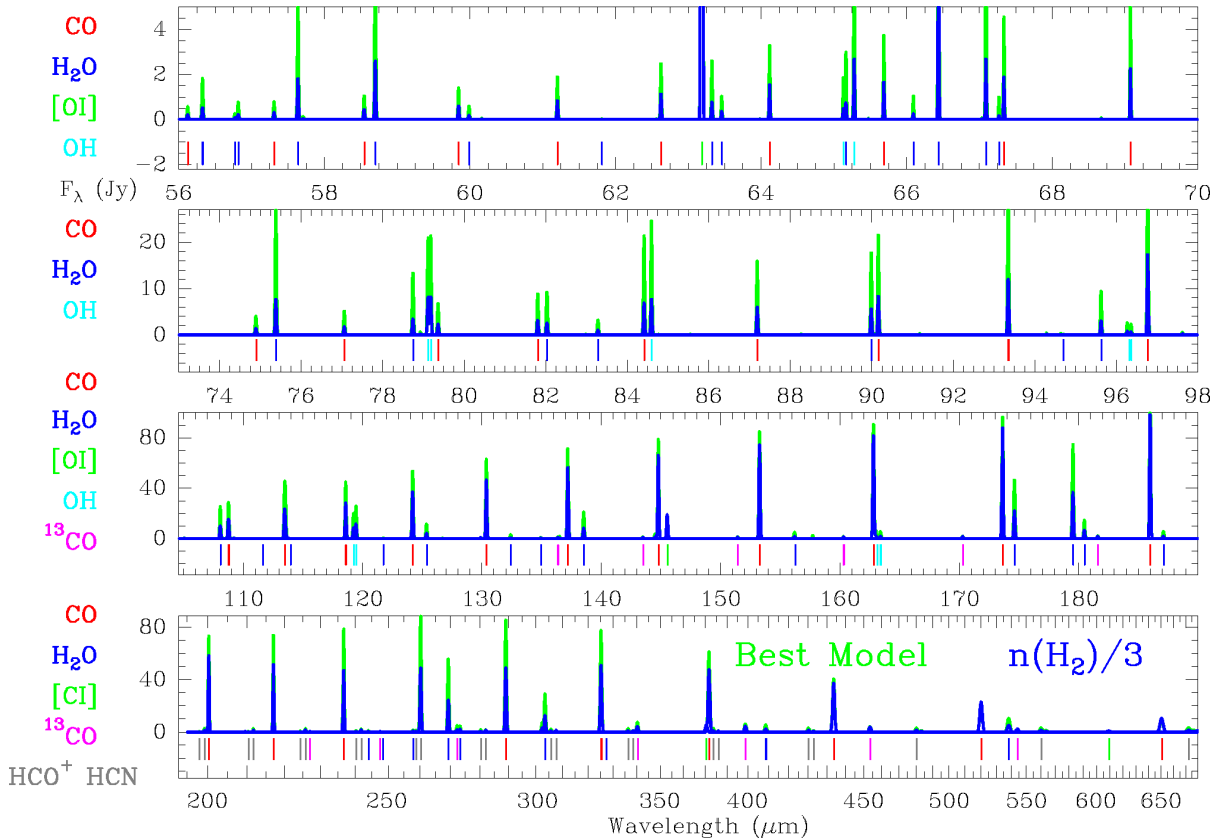


Fig. A.4. Best model discussed in the text (green curves) and a model where $n(H_2)$ is decreased by a factor 3 in all components (blue curves).